

Article

# Effects of Flow Oscillations in the Mainstream on Film Cooling

Seung Il Baek <sup>1,\*</sup> and Savas Yavuzkurt <sup>2</sup>

<sup>1</sup> Graduate Program in Acoustics, The Pennsylvania State University, University Park, PA 16802, USA

<sup>2</sup> Department of Mechanical and Nuclear Engineering, The Pennsylvania State University, University Park, PA 16802, USA; sqy@psu.edu

\* Correspondence: soongil@yahoo.co.kr

Received: 13 July 2018; Accepted: 11 October 2018; Published: 24 October 2018



**Abstract:** The objective of this study is to investigate the effects of oscillations in the main flow and the coolant jets on film cooling at various frequencies (0 to 2144 Hz) at low and high average blowing ratios. Numerical simulations are performed using LES Smagorinsky–Lilly turbulence model for calculation of the adiabatic film cooling effectiveness and using the DES Realizable *k-epsilon* turbulence model for obtaining the Stanton number ratios ( $St/St_0$ ). Additionally, multi-frequency inlet velocities are applied to the main and coolant flows to explore the effects of multi-frequency unsteady flows and the results are compared to those at single frequencies. The results show that at a low average blowing ratio ( $M = 0.5$ ) if the oscillation frequency is increased from 0 to 180 Hz, the effectiveness decreases and the Stanton number ratio increases. However, when the frequency goes from 180 to 268 Hz, the effectiveness sharply increases and the Stanton number ratio increases slightly. If the frequency changes from 268 to 1072 Hz, the film cooling effectiveness decreases and the Stanton number ratio increases slightly. If the frequency goes from 1072 to 2144 Hz, the film cooling effectiveness climbs up and the Stanton number ratio decreases. The results show that at high average blowing ratio ( $M = 1.0$ ) the trends of the film cooling effectiveness are similar to those at low blowing ratio ( $M = 0.5$ ) except from 0 to 90 Hz. If the frequency goes from 0 to 90 Hz at  $M = 1.0$ , the film cooling effectiveness increases and the Stanton number ratio decreases. It can be said that it is important to include the effects of oscillating flows when designing film cooling systems for a gas turbine.

**Keywords:** turbulent flows; numerical simulation; film cooling effectiveness; Stanton number ratio

## 1. Introduction

The gas turbine industry made an effort to increase the turbine inlet temperature and modern advanced gas turbines have a turbine inlet temperature near 1600 °C [1], which is about 200 degrees hotter than the melting point of nickel-iron alloys which are frequently used as the material of gas turbines [2]. In order to avoid damage and the thermal stresses in the inner liner material of the combustor, the material temperature should be maintained below a tolerable limit. Film cooling is one of the widely used cooling techniques to protect the gas turbine components from hot main flow gases [3].

The coolant is injected through holes on the turbine blade surface or the inner surface of the combustion chamber as shown in Figures 1 and 2. The injected coolant is bent by the main flow momentum and forms a thin coolant film on the surface resulting in the protection of the surface from the hot main flow. The film cooling reduces the adiabatic wall temperature, the temperature of the

fluid immediately above the wall under the adiabatic condition at the wall [4]. The adiabatic film cooling effectiveness  $\eta$  is defined in Equation (1).

$$\eta = \frac{(T_G - T_{aw})}{T_G - T_C} \tag{1}$$

where,  $T_{aw}$  is the adiabatic wall temperature,  $T_G$  represents the main flow temperature and  $T_C$  is the coolant temperature in Figure 3. In FLUENT,  $T_{aw}$  is calculated automatically. The node values on the boundary zones are calculated by weighted averaging of the cell data.

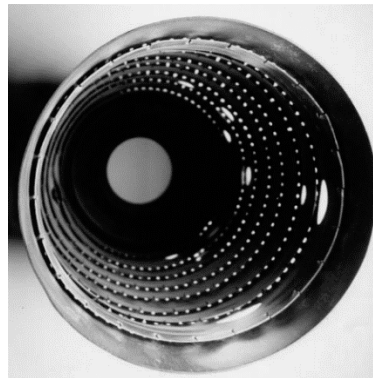


Figure 1. The inner surface of the combustion chamber showing the film cooling holes [5].



Figure 2. The turbine blade surface with film cooling holes [6].

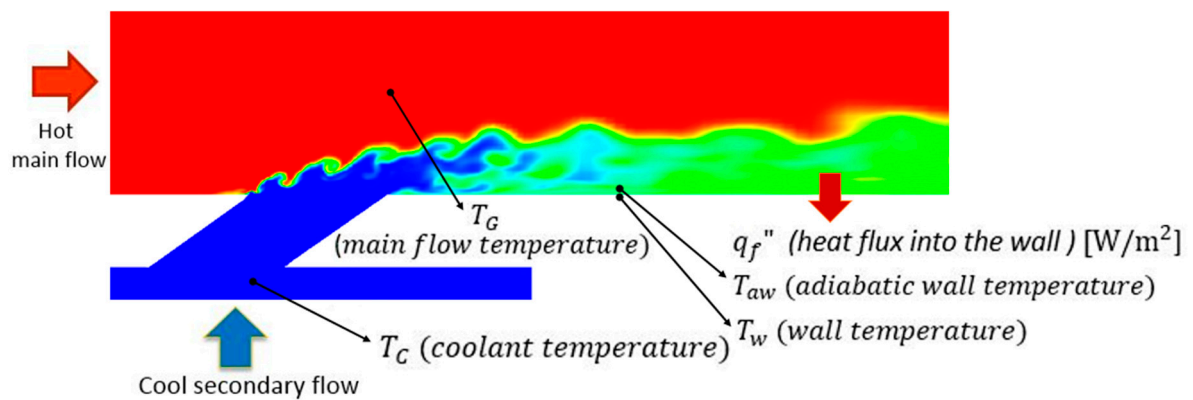


Figure 3. The temperature contours showing the coolant distribution of film cooling (Side view).

However, film cooling injection increases the Stanton number by generating high-intensity turbulence. The Stanton number ( $St_f$ ) is a non-dimensional heat transfer coefficient and is obtained using a constant heat flux on the wall. It is defined in Equation (2).

$$St_f = \frac{h_f}{\rho u C_p} \quad (2)$$

where  $\rho$  is the density,  $u$  is the flow velocity,  $C_p$  represents the specific heat of fluid, and  $h_f$  is the film heat transfer coefficient which is defined as the following:

$$h_f = q_w / (T_{aw} - T_w) \quad (3)$$

where  $q_w$  is the heat flux,  $T_{aw}$  represents the adiabatic wall temperature,  $T_w$  is the temperature of the fluid-solid interface surface as illustrated in Figure 3. The Stanton number ratio is defined as ( $St_f/St_o$ ), where  $St_o$  is the baseline Stanton number on a flat plate with no film cooling and no flow oscillations. Therefore, the Stanton number ratio ( $St/St_o$ ) shows how the Stanton numbers are affected by film cooling. As mentioned earlier, a film cooling injection increases the Stanton number by the generation of high-intensity turbulence. However, generally, the heat transfer from the hot main flow to the wall is reduced by film cooling since the effect of the increase in the Stanton number is much lower than the effect of the decrease in the adiabatic wall temperature, as shown by many experimental studies [7–9]. The film cooling performance could be evaluated in terms of the heat flux ratio which is defined in Equation (4) below [8].

$$\frac{q''_f}{q''_o} = \frac{h_f (T_{aw} - T_w)}{h_o (T_G - T_w)} = \left( \frac{St_f}{St_o} \right) \times \left( 1 - \frac{\eta}{\Phi} \right) = \frac{\text{heat flux into the wall with film cooling}}{\text{heat flux into the wall without film cooling}} \quad (4)$$

where,  $\Phi$  represents the non-dimensional metal temperature and is defined as  $\Phi = \frac{T_G - T_w}{T_G - T_C}$ , which is almost a constant value [8]. Therefore, it is important to predict the film cooling effectiveness ( $\eta$ ) and the Stanton number ratio ( $St_f/St_o$ ) accurately in order to evaluate the film cooling performance.

There have been numerous research articles on the effect of steady main flow on film cooling. However, in the film cooling flow field, the main flow is not always steady. An unsteady main flow could be induced by periodic unsteady passing wakes which are generated from the trailing edges of the stator or rotor blades in a turbine, the freestream turbulence generated in the combustion chamber, or the combustion instabilities in a combustion chamber [7,10]. Due to the generation of the wakes at the trailing edge, the exit flow of the upstream vane could be non-uniform [11]. The passing wake increases the turbulence intensity in the main flow resulting in more mixing between the main flow and the injected coolant. Thus, the adiabatic temperature on the blade surface increases and the film cooling effectiveness decreases [12]. Additionally, the Nusselt number increases because of the generation of more disturbances in the main flow. The Strouhal number ( $Sr$ ), non-dimensional frequency, of unsteady flow is proportional to the rotation speed of the blades (RPM) [12]. If the Strouhal number is increased, the film cooling effectiveness is further decreased and the Nusselt number increases [11–14]. The freestream turbulence can also affect the film cooling performance and it has a full frequency spectrum [15]. When high freestream turbulence is applied at a low blowing ratio  $M$ , ( $M = \frac{\rho_c U_c}{\rho_G U_G} = \frac{\text{injectant density} \times \text{injectant velocity}}{\text{mainstream density} \times \text{mainstream velocity}}$ ), the adiabatic film cooling effectiveness decreases because of the increased mixing between the coolant and the main flow leading to decrease of the adiabatic wall temperature [16]. Combustion instabilities have been a major concern for the gas turbine research community and designers since the instabilities cause overall gas turbine performance degradation such as flame flashback or blow off and more heat transfer to inner liners [10]. Combustion instabilities are created by a feedback cycle between heat release and acoustic oscillations [10]. Nowadays, gas turbines are often operated on lean burn premixed mode to save the fuel leading to the generation of unstable fuel and air ratios resulting in the generation of

oscillations in the heat release in the combustor. Then, the heat release disturbances excite acoustic oscillations and the generated sound radiates away from the combustion region and keeps reflections because the combustor is closed acoustically. The generated sound affects the heat release since the flame is very sensitive to acoustic sound. This sequence is repeated and a feedback cycle is created. Generally, in the combustor, the frequencies of the combustion instabilities range from 200 to 3000 Hz [17]. The instabilities consist of irregular waveforms that are expressed by the rate of heat release or oscillations in pressure as shown in Figure 4. The current study will focus on the effects of the combustion instabilities on the film cooling performance.

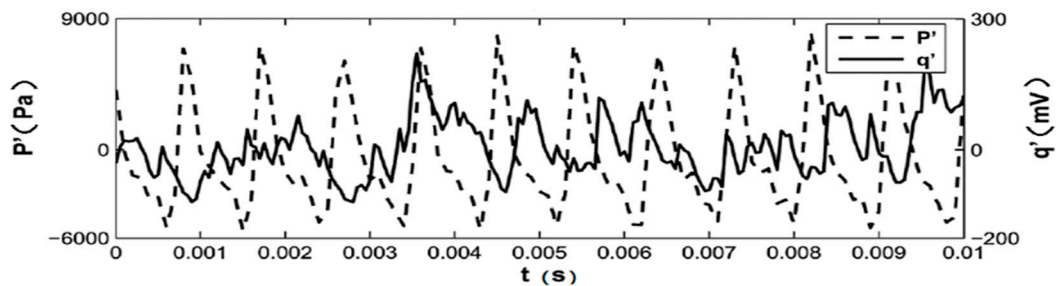


**Figure 4.** An example of the time series data of heat release ( $q'$ ) and pressure ( $p'$ ) showing instability in a combustor [18].

Computational fluid dynamics (CFD) is a cost-effective method for the study of film cooling. Strong turbulence is generated in the film cooling flow field and the turbulence needs to be modeled by Reynolds Averaged Navier–Stokes (RANS), Unsteady Reynolds Averaged Navier–Stokes (URANS), Detached eddy simulation (DES), or Large eddy simulation (LES) turbulence models. LES turbulence models predict the mixing between the hot main flow and the coolant jet better than the RANS models [19–21], even though the computational cost such as running time and storage is higher. There have been numerous studies using CFD methods to investigate the flow structures and to predict the adiabatic film cooling effectiveness and the Stanton number. Understanding the effect of the instabilities in the main flow on film cooling in the combustion chamber is critical to better design a gas turbine. However, there have been a few studies on the effect of unsteady main flow caused by the instabilities on film cooling.

Seo and Ligrani (1998) reported the effect of the main flow oscillations in a sinusoidal form at frequencies of 0, 2, 16 and 32 Hz on a flat plate experimentally [7]. The instability wave patterns in a combustion chamber are much more complicated than the simple sinusoidal form. However, the patterns of unsteady main flow velocity are more similar to the sinusoidal waveform than simple pulsations. They stated that higher frequencies of oscillation in the main flow at  $M = 0.5$  resulted in a lower adiabatic film cooling effectiveness and higher Stanton number ratio. Coulthard et al. (2000) studied the effects of cooling jet pulsing on flat plate flows experimentally [22]. They showed that pulsations applied to the coolant jet caused a lower adiabatic film cooling effectiveness at higher frequencies of pulsing and stated that the best film cooling performance was obtained at the steady coolant injection without pulsation for  $M = 0.5$ . Ekkad et al. (2006) reported the effect of coolant jet pulsations on film cooling using the blade leading edge model experimentally [23]. They discussed that the effect of jet pulsation was negligible at the blowing ratio of  $M = 0.75$ , while the film cooling effectiveness was increased and the heat transfer coefficients were slightly decreased at high blowing ratios of  $M = 1.0, 1.5,$  or  $2.0$ . They reported that a pulsing jet at the high blowing ratios of  $M = 1.0, 1.5$  and  $2.0$  weakened the coolant jet lift-off and helped the coolant to spread more laterally on the test wall, which means the jet pulsations had a positive effect on the film cooling performance at high blowing ratios. Numerically, Nikitopoulos, and Acharya (2009) showed that the film cooling performance can be improved and controlled by the coolant jet pulsing [24]. They reported that three parameters related to pulsation (frequency, blowing ratio, and duty cycle) affect the film cooling performance. El-Gabry

and Rivir (2012) investigated the effect of coolant jet pulsation on a leading edge surface experimentally and reported that the film cooling effectiveness was decreased by a factor of 2 compared to that at a steady state [25]. The blowing ratios were 1.0 and 2.0, the frequency of the pulsation was 10 Hz and the duty cycle was set as 50%. Behrendt and Gerendas (2012) discussed the effects of pressure fluctuations in the main flow caused by combustion instabilities on the cooling performance of double skin perforated liners at high blowing ratios of  $M = 1.7$  to 5.8 experimentally [26]. They showed that the pressure oscillations decreased the cooling effectiveness considering the effects of the conduction through the wall material. They stated that the cooling effectiveness of the wall material with a low thermal conductivity was more affected by the pressure oscillations, indicating the importance of conjugate heat transfer.

The current study investigates the effects of oscillations in the main flow and coolant jet on film cooling on a flat plate geometry with an inline cylindrical hole with a  $35^\circ$  inclined injection angle for average blowing ratios of  $M = 0.5$  and 1.0 using numerical simulations. The main purpose is to observe the effect of unsteady mainstream flow on the adiabatic film cooling effectiveness and the Stanton number at various frequencies (0 to 2144 Hz) and to understand and explain the results based on fundamental processes. A real combustion chamber has a more complex geometry than a flat plate, however, the results from a simple geometry like the flat plate could be applied to a complex geometry with some corrections [11]. Further, multi-frequency velocities obtained from the data of gas turbine combustion chamber instabilities are applied to the main and coolant flow using the Fourier Series and the results are compared to those at single frequencies in order to see what would happen if real conditions with many frequencies are applied.

## 2. Test Cases

This study investigates the effects of oscillations in the main flow and the coolant jet on film cooling on a flat plate at average blowing ratios of  $M = 0.5$  and 1.0. For validation, experimental data at frequencies of 0, 2, 16, and 32 Hz for  $M = 0.5$  from Seo et al. [7] and experimental data at 0 and 32 Hz for  $M = 1.0$  from Seo et al. [27] are chosen for comparisons with the numerical results. The geometry and the operating conditions are taken from Seo et al. [7]. A three-dimensional mesh is used for this study and the computational domain is illustrated in Figure 5. The computational domain extends 24 hole diameters downstream from the cooling hole center. The black dashed line represents the domain including a full hole, consisting of 2.04 million structured hexahedron cells for LES and DES calculations. Figures 6 and 7 show the side view of the mesh and the close-up side view of the mesh near the coolant injection region respectively. In Figure 6, the black regions represent fine grid zones, where complicated flow fields are generated by the interaction between the mainstream and the coolant jet and the boundary layer regions. Boundary conditions for the computational domain are shown in Table 1. The boundary condition for outflow is a steady uniform pressure outlet with a gauge pressure of 0 pascals. In the streamwise direction, the mesh spacing values range from 6 near the cooling hole to 35 near the end of the domain in  $x^+$  units ( $x^+ = \frac{x}{\nu} \sqrt{\frac{\nu U}{y}}$ ). In the spanwise direction, the mesh spacing values are about 20 throughout the domain in  $z^+$  units ( $z^+ = \frac{z}{\nu} \sqrt{\frac{\nu U}{y}}$ ). In the wall normal direction, the value of  $y^+$  ( $y^+ = \frac{y}{\nu} \sqrt{\frac{\nu U}{y}}$ ) of the first cell above the wall was about 1 and 25 cell layers are made up to  $y^+ = 30$  in order to capture the wall normal velocity gradient in the viscous sublayer and other near wall features accurately. The hole diameter of the cylindrical tube is 0.025 m, the ratio of the tube length to the hole diameter ( $L/D$ ) is 1.6, the inline injection angle is  $35^\circ$ , and the ratio of pitch to hole diameter ( $P/D$ ) is 3. Five film cooling holes are placed in a row in the experiment. However, a mesh having a single hole is used to reduce the computational costs. The initial turbulence intensity of the main flow is 0.2% and the oscillations in the main flow would not be affected by the initial turbulence intensity because the level of free stream turbulence 0.2% is considered to be very low. The mainstream velocity is 10 m/s, the temperature of the main flow is 300 K and the coolant temperature is 293 K.

The Freestream Reynolds number is based on the freestream velocity  $U_G$  and hole diameter  $D$ ,  $Re_D$  is 16,005. ( $Re_D = \frac{DU_G}{\nu}$ ).

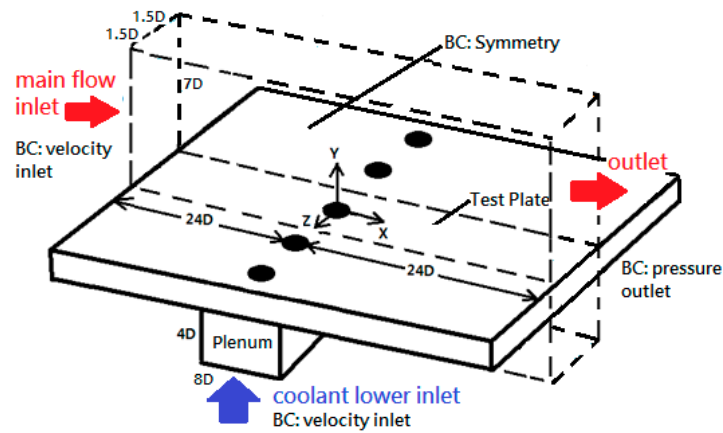


**Figure 5.** The schematic of the computational domain for LES (Large eddy simulation) and DES (Detached eddy simulation) calculations for the Seo et al. [7] case.

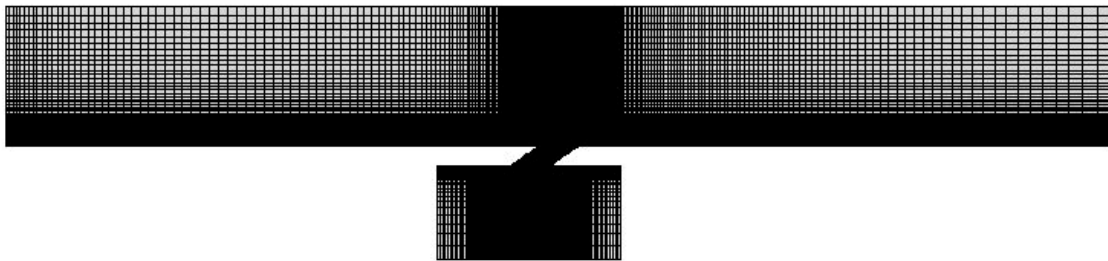


**Figure 6.** The CFD (Computational fluid dynamics) mesh reproducing the Seo et al. [7] case.

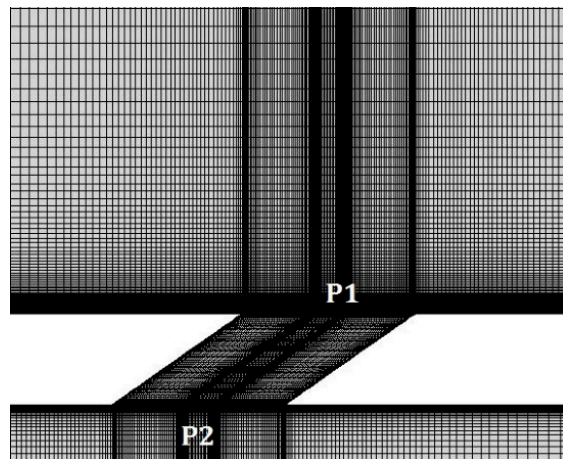


**Figure 7.** A close-up of the mesh near the injection region of the Seo et al. [7] case.

**Table 1.** The boundary conditions for the computational domain [28].

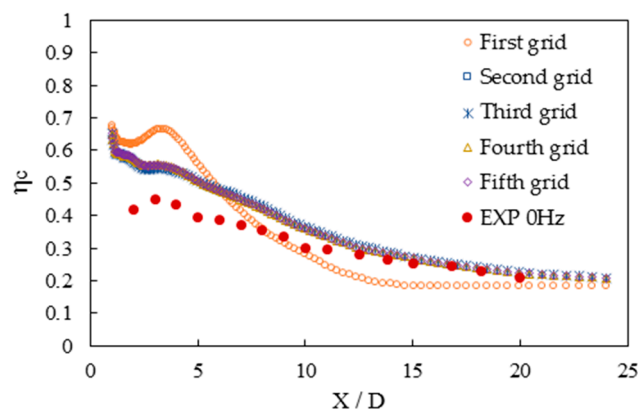
Surface	Boundary Condition
Main inlet	Velocity inlet
Coolant lower inlet	Velocity inlet
Top	Symmetry
Test wall	Wall
Outflow	Pressure outlet
Main sides	Symmetry
Sides of plenum	Wall
Delivery tube	Wall

Figure 8 illustrates the results of a mesh sensitivity study for the steady case. In Figure 8,  $\eta_c$  is the adiabatic film cooling effectiveness at the centerline ( $z = 0, y = 0$ ) for the steady case (0 Hz) and  $M = 0.5$ . Results are obtained using LES Smagorinsky–Lilly turbulence model. Five different grids are investigated and the descriptions of the grids used are shown in Table 2. It is found that the third grid with 2.04 million cells shows almost the same result for the centerline film cooling effectiveness as the two finer meshes of the fourth and the fifth grids. Therefore, the mesh with 2.04 million cells is used in all LES calculations to obtain the film cooling effectiveness. At the main flow and the plenum coolant inlets, the velocity inlet is used as the boundary condition and uniform velocity profiles are applied as the experiment. The velocity at the main flow inlet is set as the following:

$$V_{\text{main\_inlet}} = A \sin(2\pi ft) + 10 \text{ m/s} \tag{5}$$

where 10 corresponds to the velocity at the steady state. A values and the amplitudes of the main flow velocity oscillation are taken from Seo et al. [7] and available up to 32 Hz. They are illustrated in Table 3. In the table, A values are shown as a function of frequency ( $f$ ) and the Strouhal number ( $Sr$ ). The Strouhal number ( $Sr$ )—the non-dimensional frequencies—are defined as the following:

$$Sr = \frac{2\pi f D}{U_G} = \frac{\text{angular frequency} \times \text{hole diameter}}{\text{mainstream velocity}} \tag{6}$$



**Figure 8.** The grid Sensitivity Study for the LES calculation.

**Table 2.** The specifications of grid arrangements in the cross-flow block for the grid sensitivity study.

Grid	Number of Cells in X Direction	Number of Cells in Y Direction	Number of Cells in Z Direction	Number of Cells in Cross-Flow Block	Number of Total Cells
First	320	50	32	0.52 million	1.14 million
Second	334	60	48	0.98 million	1.6 million
Third	352	80	50	1.42 million	2.04 million
Fourth	364	94	56	1.94 million	2.56 million
Fifth	390	110	64	2.78 million	3.4 million

**Table 3.** The values of A up to 32 Hz in Equation (5) as a function of frequency [7].

Frequency (f) (Hz)	0	2	16	32
Strouhal number (Sr)	0	0.03142	0.25133	0.50265
A	0	1.82	0.57	0.44

The velocity at the coolant plenum inlet is expressed as

$$V_{\text{plenum\_inlet}} = B \sin(2\pi ft + \alpha) + 0.164 \text{ m/s} \tag{7}$$

where 0.164 corresponds to the velocity at the steady state for  $M = 0.5$  and  $\alpha$  is the phase difference between the main flow velocity oscillation at the main inlet and the coolant flow velocity oscillation at the plenum inlet. In this study, no phase difference ( $\alpha = 0$ ) is assumed since the phase difference ( $\alpha$ ) only affects a very narrow region near the hole, as illustrated in Figure 9. The LES results showed how, when the phase difference ( $\alpha$ ) was 0,  $\pi/4$  or  $\pi/2$ , there was no difference in the film cooling centerline effectiveness for  $X/D > 4$ . The B values, amplitudes of the coolant flow velocity oscillation, are shown in Table 4. B values are not given in Seo et al. [7] but  $P_2$ - $P_1$  static pressure variation plots in terms of time were provided where  $P_1$  and  $P_2$  represent the static pressure around the hole exit and the tube inlet, respectively, as shown in Figure 7.

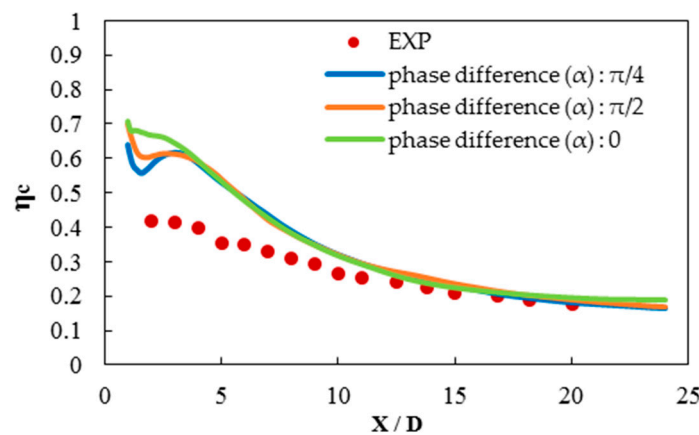


**Figure 9.** The effect of phase difference between the mainflow and coolant oscillation for  $M = 0.5$ , 2 Hz using FLUENT, LES, Smagorinsky–Lilly.

**Table 4.** The B values in Equation (7) as a function of frequency.

Frequency (f) (Hz)	0	2	16	32
Strouhal number (Sr)	0	0.03142	0.25133	0.50265
B	0	0.04	0.05	0.16

B values were obtained by the FLUENT code using the given  $P_2$ - $P_1$  values in plots employing a “trial and error” technique. By guessing B values in Equation (7), the values were adjusted to match the  $P_2$ - $P_1$  values. The experimental data from Seo et al. [7] is available up to 32 Hz and no other data at higher frequencies is available at this point. However, the combustion instability frequencies range from 200 to 3000 Hz [17]. The data at higher frequencies than 32 Hz are obtained by using extrapolation. Although the  $P_2$ - $P_1$  plots are not perfectly sinusoidal, they can be fitted with the following sinusoidal form in Equation (8) satisfactorily.

$$P_2 - P_1 = C \sin(2\pi ft) + D \tag{8}$$

Figure 10 illustrates the C and D values in terms of frequency and it is found that C and D values up to 32 Hz are approximately linear with the frequency in a log-log plot. Therefore, C and D values at higher frequencies than 32 Hz are extrapolated by using this linear characteristic. Then, A and B values up to 2144 Hz in Equations (5) and (7) are obtained by the FLUENT code using the “trial and error” technique, which means A and B values are adjusted to match plots of the Equation (8) by guessing the A and B values. A and B values at various frequencies from 90 to 2144 Hz are shown in Table 5. As discussed later, small variations of the A and B values in Equations (5) and (7) have little effect on the determination of the film cooling effectiveness because at high frequencies the film cooling effectiveness is dominated by the oscillating frequency and the convection speed of the vortices (main flow speed). Therefore, it could be justified that the C and D values in Equation (8) at high frequencies are extrapolated by using the linear characteristic as shown in Figure 10. Further, since no data is available at these frequencies, in this case, this is the best that can be done and can be corrected if the future data shows that it is not correct. Although everything is not resolved, it is a start and will help future researchers who would like to study this topic. The results here can help them to open many areas that can be investigated.

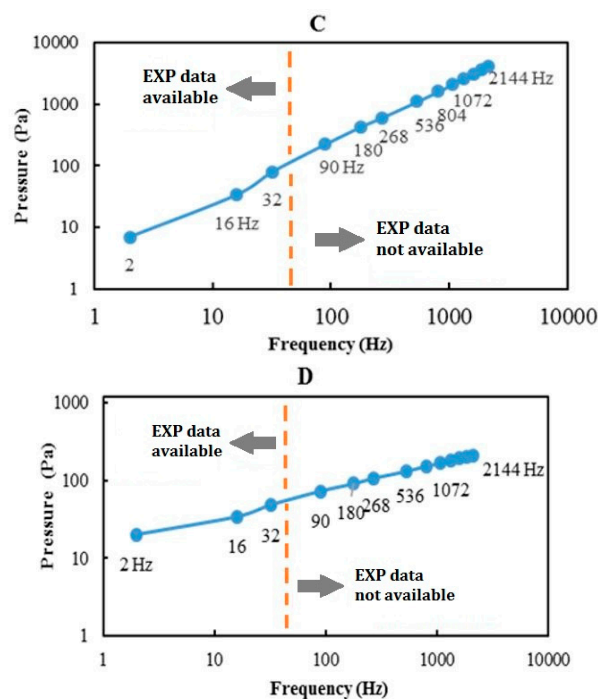


**Figure 10.** The values of C and D up to 2144 Hz in Equation (8) as a function of frequency obtained from extrapolation.

**Table 5.** The A and B values from 90 to 2144 Hz in Equations (5) and (7) as a function of frequency.

Frequency (Hz)	Sr	A	B
90	1.41372	0.37	0.176
180	2.82743	0.32	0.187
268	4.20973	0.29	0.194
536	8.41947	0.23	0.203
804	12.6292	0.2	0.209
1072	16.8389	0.19	0.211
1340	21.0487	0.185	0.213
1608	25.2584	0.18	0.215
1876	29.4681	0.175	0.217
2144	33.6779	0.17	0.22

### 3. Numerical Modeling

Numerical simulations are carried out using LES Smagorinsky–Lilly model for the film cooling effectiveness and using the DES Realizable *k-epsilon* model for the Stanton number ratios ( $St_f/St_o$ ). The Large Eddy Simulation (LES) approach resolves large-scale eddies of the turbulent flow while it models small-scale eddies. Unsteady Reynolds-Averaged Navier–Stokes Equations (URANS) approach models all turbulence length scales and solves for ensemble-averaged quantities for unsteady flow. The Detached Eddy Simulation (DES) model is a hybrid turbulence model of unsteady RANS and LES models. It works as unsteady RANS models in the boundary layer region whereas a LES model is employed in the freestream region. The computational costs in DES calculations are less than those in LES but still greater than those in the RANS calculations. All governing equations are marched using second order implicit schemes. For pressure-velocity coupling, the SIMPLE algorithm is used.

Generally, URANS results over-predict the film cooling effectiveness and the Stanton number compared to the experimental data while the LES results show more accurate predictions and LES can simulate the problem's physics better [19,29]. The over-prediction is attributed to low mixing predicted between the mainstream and the coolant compared to the experiment. Even though URANS results can be obtained much faster (over about 20 times) than the LES simulations, commercial URANS turbulence models have a limitation to exactly predict the interaction between the mainstream and the coolant jet since it is associated with the anisotropic turbulence [20]. Additionally, it was shown that the LES Smagorinsky–Lilly showed the best results for film cooling effectiveness compared with the results by other LESs [19].

In this study, the Stanton number ratios are obtained using DES calculations instead of LES because LES results for the Stanton number ratios are not ready at this point in time. Good results in the Stanton number ratio are strongly dependent on the prediction of the turbulence in the near wall region while it is important to predict various flow structures generated by the interaction between the mainstream flow and the coolant jet in order to obtain the film cooling effectiveness accurately [30]. Therefore, a mesh with very high resolution near the wall region is necessary for LES calculations and the computational cost will be much expensive since this mesh requires a much longer run time. LES results for the Stanton number ratios are not ready at this point in time. In the current study, the grid used to obtain the Stanton number ratio by using DES calculations is the same mesh used to obtain the film cooling effectiveness by using LES simulations. DES results show better predictions than the URANS results even though they are not better than LES results [31]. In the current study, ANSYS FLUENT v.14 [32] is used for the CFD calculations and Pointwise v.16 [33] is used for mesh generation. For LES calculations, the time step was between  $4.0 \times 10^{-6}$  s and  $1.0 \times 10^{-5}$  s depending on the frequency. The time step of  $1.0 \times 10^{-5}$  s corresponds to the time for the main flow to convect the length equal to the hole diameter with 250 time steps [34], and the time step was decreased as the frequency increased. After statistically steady state conditions were achieved, the statistics were collected for multiples of oscillation period over at least 0.25 s [35]. Especially, the statistics were accumulated for 1.0 s for 2 Hz oscillation. For each time step, 10–20 sub-iterations which are additional explicit pseudo time steps are performed in order to make sure that the data at each physical time step is well resolved [21]. For LES calculations, the run time was about 2–3 months by using 16 cores of the Intel Xeon E5-2665 processor. For DES calculations, the time step was  $1.0 \times 10^{-5}$  s [36] and the run time was about 3 weeks.

#### 3.1. Governing Equations and Turbulence Models

In this study, it is assumed that the fluid is Newtonian, incompressible, with temperature dependent variable properties. The compressibility effects are negligible and the incompressible Navier–Stokes equations can be used because the main flow velocity is 10 m/s (Mach 0.029) and the averaged coolant injection velocity is 5 m/s (Mach 0.015) [37]. The governing equations consist of the continuity, the momentum, and the energy equations.

### 3.2. Unsteady Reynolds-Averaged Navier-Stokes Equations (URANS) Approach

The Navier–Stokes equations are the conservation of momentum and the continuity equations in differential form. RANS approach ensemble-averages all turbulent fluctuations in the flow. In this study, an unsteady RANS approach was used because unsteady flow structures could be predicted only by unsteady turbulence models, such as Unsteady RANS, LES, or DES. The ensemble averages of conservation of mass (Equation (9)), momentum (Equations (10)–(12)) and energy Equations (Equation (13)) for turbulent flows are expressed as follows [38–40]:

Conservation of Mass (Continuity equation):

$$\frac{\partial \rho}{\partial t} + \nabla \cdot (\rho \bar{u}) = 0 \tag{9}$$

Conservation of Momentum:

$$\frac{\partial(\rho \bar{u})}{\partial t} + \nabla \cdot (\rho \bar{u} \bar{u}) = -\frac{d\bar{p}}{dx} + \nabla \cdot (\mu \nabla u) + \left\{ -\frac{\partial(\rho \overline{u'u'})}{\partial x} - \frac{\partial(\rho \overline{u'v'})}{\partial y} - \frac{\partial(\rho \overline{u'w'})}{\partial z} \right\} \tag{10}$$

$$\frac{\partial(\rho \bar{v})}{\partial t} + \nabla \cdot (\rho \bar{v} \bar{u}) = -\frac{d\bar{p}}{dy} + \nabla \cdot (\mu \nabla v) + \left\{ -\frac{\partial(\rho \overline{v'u'})}{\partial x} - \frac{\partial(\rho \overline{v'v'})}{\partial y} - \frac{\partial(\rho \overline{v'w'})}{\partial z} \right\} \tag{11}$$

$$\frac{\partial(\rho \bar{w})}{\partial t} + \nabla \cdot (\rho \bar{w} \bar{u}) = -\frac{d\bar{p}}{dz} + \nabla \cdot (\mu \nabla w) + \left\{ -\frac{\partial(\rho \overline{w'u'})}{\partial x} - \frac{\partial(\rho \overline{w'v'})}{\partial y} - \frac{\partial(\rho \overline{w'w'})}{\partial z} \right\} \tag{12}$$

Conservation of Energy:

$$\rho c_p \frac{D\bar{T}}{Dt} = k \nabla^2 T - \rho c_p \frac{\partial \overline{T'u'}}{\partial x} - \rho c_p \frac{\partial \overline{T'v'}}{\partial x} - \rho c_p \frac{\partial \overline{T'w'}}{\partial x} \tag{13}$$

Six Reynolds stresses,  $-\rho \overline{u'u'}$ ,  $-\rho \overline{u'v'}$ ,  $-\rho \overline{u'w'}$ ,  $-\rho \overline{v'v'}$ ,  $-\rho \overline{v'w'}$  and  $-\rho \overline{w'w'}$  in Equations (10)–(12) and  $\overline{T'u'}$ ,  $\overline{T'v'}$  and  $\overline{T'w'}$  in Equation (13) need to be modeled [38]. The overbar represents the mean components and  $u'$ ,  $v'$ ,  $w'$  and  $T'$  are fluctuating velocity components and the temperature. A closure for the equations could be obtained through the Boussinesq hypothesis, which is expressed as follows [40]:

$$-\rho \overline{u'_i u'_j} = \mu_t \left( \frac{\partial u_i}{\partial x_j} + \frac{\partial u_j}{\partial x_i} - \frac{2}{3} \frac{\partial u_k}{\partial x_k} \delta_{ij} \right) - \frac{2}{3} \rho k \delta_{ij} \tag{14}$$

where,  $\mu_t$  is the turbulent viscosity and needs to be modeled as the following [40]:

$$\mu_t = \frac{\rho C_\mu k^2}{\varepsilon} \tag{15}$$

The turbulent viscosity  $\mu_t$  is assumed to be the same in all directions and shows good results for many simple turbulent flows even though the assumption is not generally true [40]. The Equations (9)–(13) cannot be solved analytically. Thus, CFD is the only method to obtain solutions of the equations and requires a turbulence model in order to close the equation mathematically. In this study, the Realizable  $k-\varepsilon$  model was used for DES calculations and “Realizable” means this turbulence model satisfies certain mathematical constraints for Reynolds stresses which are consistent with a turbulent flow physics [41]. The Realizable  $k-\varepsilon$  model has the same equation of the turbulent kinetic energy as the standard  $k-\varepsilon$  model, though this model uses an improved equation for turbulent dissipation rate ( $\varepsilon$ ). The Realizable  $k-\varepsilon$  model predicts the spreading rate of both round and planar jets more accurately than other URANS models and is suitable for flows having a large rotation, strain rate, and recirculation and flows with separation and high-pressure gradients [32].

The turbulent kinetic energy  $k$  transport equation is expressed as follows [42]:

$$\frac{\partial(\rho k)}{\partial t} + \frac{\partial(\rho k u_i)}{\partial x_i} = \frac{\partial}{\partial x_i} \left\{ \left( \mu + \frac{\mu_t}{\sigma_k} \right) \frac{\partial k}{\partial x_j} \right\} + G_k + G_b - \rho \epsilon - Y_M + S_k \quad (16)$$

The turbulent dissipation rate  $\epsilon$  transport equation is set as the following [42]:

$$\frac{\partial(\rho \epsilon)}{\partial t} + \frac{\partial(\rho \epsilon u_i)}{\partial x_i} = \frac{\partial}{\partial x_i} \left\{ \left( \mu + \frac{\mu_t}{\sigma_\epsilon} \right) \frac{\partial \epsilon}{\partial x_j} \right\} + \rho C_1 S_\epsilon - \frac{C_2 \rho \epsilon^2}{k + \sqrt{\nu \epsilon}} + \frac{\epsilon}{k} C_{1\epsilon} C_{3\epsilon} G_b + S_\epsilon \quad (17)$$

where,  $C_1 = \max \left[ 0.43, \frac{\sqrt{2s_{ij}S_{ij}^k}}{\frac{\epsilon}{\sqrt{2s_{ij}S_{ij}^k} + 5}} \right]$ ,  $C_3 = \tanh \left| \frac{\nu}{u} \right|$ .  $G_k$ ,  $G_b$  represent the turbulent kinetic energy production terms because of the mean velocity gradient and buoyancy, respectively.  $Y_M$  is the dilatation dissipation term to prevent the over-prediction of  $s$  the spreading rate in a compressible flow. The model constants are 1.44,  $C_2 = 1.9$ ,  $C_{1\epsilon} = 1.0$ , 1.2.  $S_k$  and  $S_\epsilon$  represent user-defined source terms. In the plot of  $U^+$  ( $U^+ = U \sqrt{\frac{\nu}{vU}}$ ) versus  $Y^+$ , the mean velocity profiles in the inner region of the boundary layer obtained by using the Realizable  $k$ - $\epsilon$  model are well represented by the law of the wall and the logarithmic law.

### 3.3. Large Eddy Simulation (LES) Approach

The Large Eddy Simulation (LES) resolves large eddies directly, whereas small eddies are modeled. Direct Numerical Simulation (DNS) resolves the whole turbulent scales and no modeling is necessary, however, the computational cost for DNS is too expensive and DNS requires a much finer mesh than LES. Therefore, DNS is still not feasible for the flows with high Reynolds number. LES filters out the eddies whose length scales are smaller than grid spacing and LES only resolves large eddies, however, this is reasonable since mass, energy, and momentum are mostly transported by large eddies. Additionally, large eddies are non-isotropic and are strongly dependent on the geometry and the boundary conditions while small eddies are nearly isotropic except very near walls and thin shear layers and are less dependent on the geometry [32]. Therefore, the LES model requires a finer mesh than the RANS model. LES calculations have to be run for a long flow time to reach statistically steady state conditions and its computational cost is much higher than that of RANS calculations in terms of the memory requirements and CPU time. Filtered Navier–Stokes equations for LES calculations are expressed as the following [32]:

$$\frac{\partial \rho}{\partial t} + \frac{\partial}{\partial x_i} (\rho \bar{u}_i) = 0 \quad (18)$$

$$\frac{\partial(\rho \bar{u})}{\partial t} + \frac{\partial}{\partial x_j} (\rho \bar{u}_i \bar{u}_j) = \frac{\partial}{\partial x_j} \left[ \mu \left( \frac{\partial \bar{u}_i}{\partial x_j} + \frac{\partial \bar{u}_j}{\partial x_i} \right) - \frac{2}{3} \mu \frac{\partial \bar{u}_l}{\partial x_l} \delta_{ij} \right] - \frac{d\bar{p}}{dx} + \frac{\partial \tau_{ij}}{\partial x_j} \quad (19)$$

where,  $\tau_{ij}$  is the sub-grid scale turbulent stress and it is expressed as the following:

$$\tau_{ij} = \rho \overline{u_i u_j} - \rho \bar{u}_i \bar{u}_j \quad (20)$$

The sub-grid scale turbulent stress ( $\tau_{ij}$ ) needs modeling as the following and the Boussinesq hypothesis is employed like the RANS models [32].

$$\tau_{ij} - \frac{1}{3} \tau_{kk} \delta_{ij} = -2\mu_t \bar{S}_{ij} \quad (21)$$

where,

$$\bar{S}_{ij} = \frac{1}{2} \left( \frac{\partial \bar{u}_i}{\partial x_j} + \frac{\partial \bar{u}_j}{\partial x_i} \right) \quad (22)$$

$\mu_t$  is the subgrid-scale turbulent viscosity and  $\overline{S_{ij}}$  represents the rate of strain tensor for the resolved scale. In the current study, the Smagorinsky–Lilly model was used and the turbulent viscosity is modeled as the following:

$$\mu_t = \rho L_s^2 \sqrt{2\overline{S_{ij}} \overline{S_{ij}}} \tag{23}$$

where,  $L_s$  represents the mixing length for the subgrid scales and is calculated as the following [32]:

$$L_s = \min(\kappa d, C_s \Delta) \tag{24}$$

where,  $\kappa$  is the von Karman’s universal constant whose typical value is 0.41,  $d$  is the distance to the closest wall,  $C_s$  represents the Smagorinsky constant, and  $\Delta$  represents the local grid scale [43].

### 3.4. Fourier Analysis of the Combustion Instability Data

Unstable fuel/air ratios create disturbances in a gas turbine combustor during operation on lean premixed mode [44]. Combustion instabilities could be expressed by oscillations in flow rate, pressure, or heat release [10]. Experimentally measured pressure oscillations as a function of time in a combustor are illustrated in Figure 11 and the data consists of irregular waveforms.

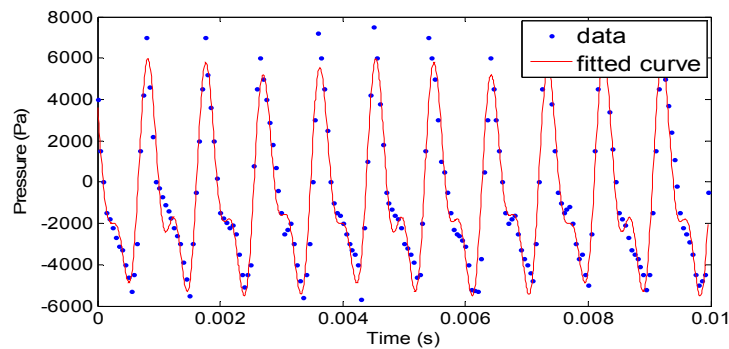


**Figure 11.** An example of time series data of pressure ( $p'$ ) showing instability in a combustor [18] and the curve fit obtained using Fourier transforms [28].

The current study discusses the effects of oscillations and covers the full frequency range of the combustion instabilities. Various frequencies (268, 536, 804, 1072, 1340, 1608, 1876, and 2144 Hz) were identified as the dominant frequencies from a Fourier analysis of the experimental combustor instability data in Figure 11 by using MATLAB. Small humps of the red fitted curve at 0.0015 s, 0.005 s, and 0.0087 s in Figure 11 are acceptable because their pressure amplitudes are low and they have little effect on the determination of the dominant frequencies.

The resulting equation for pressure is expressed by Equation (25) and Table 6 [28].

$$P = -536 + \sum_{n=1}^8 \left[ \begin{array}{l} c_n \cos(2\pi \times 268 \times n \times t) \\ + s_n \sin(2\pi \times 268 \times n \times t) \end{array} \right] \tag{25}$$

**Table 6.** The coefficients at dominant frequencies [28].

Frequency (Hz)	n	Coefficients for Cosine Terms (Cn)	Coefficients for Sine Terms (Sn)
268	1	60	115
536	2	24	52
804	3	−286	30
1072	4	3993	−1364
1340	5	263	−141
1608	6	190	74
1876	7	−124	151
2144	8	18	−2207

In Figure 11, the curve fit is given in Equation (25) shows a good match to the experimental data. Under-prediction of the peak pressures is acceptable since it has little effect to determine dominant frequencies. However, Equation (25) cannot be directly used in the CFD simulation for this study because the experimental geometry and operating conditions such as blowing ratio, flow velocity, and turbulent intensity are different from those of the current study. Instead, the pressure Equation (25) could be used to determine the dominant frequencies to form velocities at the main inlet and the plenum inlet and could be used for calculating the weights at each dominant frequency. The weights at each dominant frequency are used to create realistic multi-frequency inlet velocities under the current operating conditions. The weights for cosine terms ( $WC_m$ ) and sine terms ( $WS_m$ ) are calculated by Equations (26) and (27), respectively, and the values are seen in Table 7 [28].

$$WC_m = \frac{|C_m|}{\sum_{n=1}^8 |C_n|} \tag{26}$$

$$WS_m = \frac{|S_m|}{\sum_{n=1}^8 |S_n|} \tag{27}$$

**Table 7.** The weights at the dominant frequencies [28].

Frequency (Hz)	m	Weight for Cosine Terms (WCm)	Weight for Sine Terms (WSm)
268	1	0.0121	0.02782
536	2	0.00484	0.01258
804	3	0.05768	0.00726
1072	4	0.80537	0.3299
1340	5	0.05304	0.03411
1608	6	0.03832	0.0179
1876	7	0.02501	0.03653
2144	8	0.00363	0.53387

The following velocities are applied to both the main and the coolant plenum inlets using the weights for each dominant frequency in Table 6. Thus, the flow velocities at the main inlet ( $V_{main\_inlet}$ ) and the coolant plenum inlet ( $V_{plenum\_inlet}$ ) are expressed as the following [28]:

$$V_{main\_inlet} = 10 + 0.29 \times wc1 \times \cos(2\pi \times 268t) + 0.29 \times ws1 \times \sin(2\pi \times 268t) + \dots + 0.17 \times wc8 \times \cos(2\pi \times 2144t) + 0.17 \times ws8 \times \sin(2\pi \times 2144t) \text{ (m/s)} \tag{28}$$

$$V_{plenum\_inlet} = 0.164 + 0.194 \times wc1 \times \cos(2\pi \times 268t) + 0.194 \times ws1 \times \sin(2\pi \times 268t) + \dots + 0.22 \times wc8 \times \cos(2\pi \times 2144t) + 0.22 \times ws8 \times \sin(2\pi \times 2144t) \text{ (m/s)} \tag{29}$$

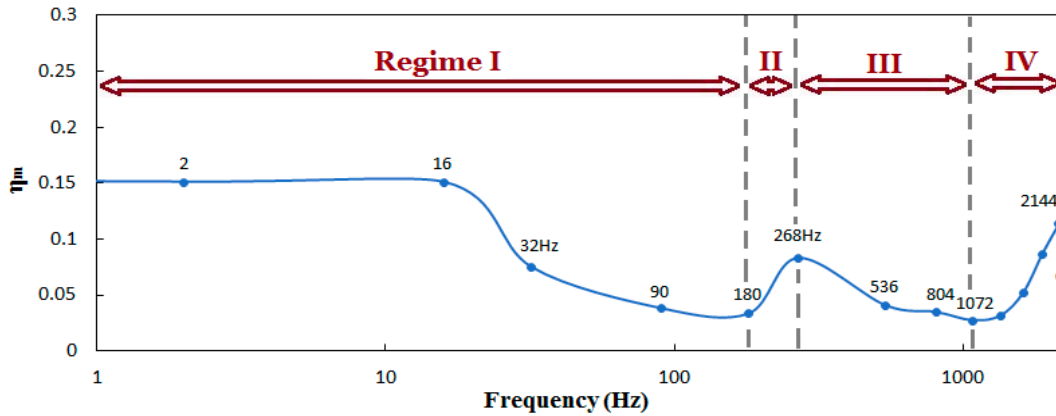
where 10 and 0.164 correspond to the main flow inlet and coolant plenum inlet velocities at the steady state, respectively. The values 0.29, . . . , 0.17 and 0.194, . . . , 0.22 correspond to the values of A and B at each dominant frequency in Equations (5) and (7) as given in Table 5.

## 4. Results and Discussion

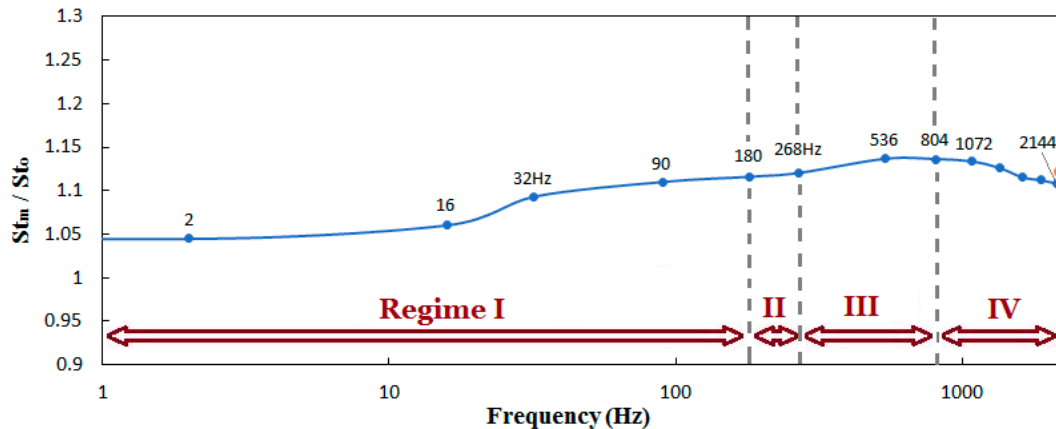
### 4.1. Average Blowing Ratio of $M = 0.5$

Figure 12 illustrates the results of the spanwise-averaged film cooling effectiveness at  $X/D = 7$  as a function of frequency at the average blowing ratio of  $M = 0.5$ . Based on this figure, four distinct regimes (Regime I, II, III, and IV) could be identified for the behavior of the adiabatic film cooling effectiveness. When the oscillation frequency rises from 0 to 180 Hz (Regime I), the effectiveness decreases while when the frequency climbs from 180 to 268 Hz (Regime II), the effectiveness is sharply increased. However, when the frequency is increased from 268 to 1072 Hz (Regime III), the effectiveness drops, whereas when the frequencies exceed 1072 Hz (Regime IV), the effectiveness increases. Figure 13

shows the results of the spanwise-averaged Stanton number ratio at  $X/D = 7$  as a function of frequency at the average blowing ratio of  $M = 0.5$ . In the Regime I, II, and III, which are identified by the behavior of the film cooling effectiveness in Figure 12, if the frequency rises, the Stanton number ratio increases. However, in Regime IV, when the oscillation frequency increases, the Stanton number ratio decreases. The details will be discussed later in the manuscript.



**Figure 12.** The variation of the spanwise-averaged effectiveness in terms of frequency (Hz) at  $X/D = 7$  for  $M = 0.5$  obtained by FLUENT, LES, Smagorinsky–Lilly model. The orange color point is the result for the multi-frequency unsteady flow. It represents the spanwise-averaged film cooling effectiveness when Equations (28) and (29) are used instead of individual frequencies [28].



**Figure 13.** The variation of the spanwise-averaged Stanton number ratio in terms of frequency (Hz) at  $X/D = 7$  for  $M = 0.5$  obtained by the FLUENT, DES, Realizable  $k$ -epsilon model. The orange color point is the result for the multi-frequency unsteady flow. It represents the spanwise-averaged Stanton number ratio when Equations (28) and (29) are used instead of individual frequencies.

#### 4.2. Regime I for $M = 0.5$ : 0–180 Hz

##### 4.2.1. Film Cooling Effectiveness

When the frequencies of the main flow and the coolant jet goes from 0 to 180 Hz at the average blowing ratio of  $M = 0.5$ , the centerline and the spanwise-averaged effectiveness decrease, as seen in Figures 14 and 15 respectively. As illustrated in Figure 12, the spanwise-averaged film cooling effectiveness at  $X/D = 7$  shows a slight decrease between 0 and 16 Hz and a large decrease between 16 and 32 Hz. If the oscillation frequency is increased up to 16 Hz, the mixing of the coolant with the hot mainstream fluid increases, however, as seen in Figure 16(a1–e1), the coolant almost stays attached to the wall leading to a slight decrease of the film cooling effectiveness. As seen in Table 4, the amplitude of the coolant velocity oscillation at the plenum inlet increases remarkably at 32 Hz, resulting in

jet lift-off at the high-velocity magnitude part of the cycle and entrainment of hot main flow under the cooling jet as shown in Figure 16(a2–e2). Therefore, the centerline and the spanwise-averaged effectiveness decreases significantly from 16 to 32 Hz. As shown in Figure 12, the spanwise-averaged effectiveness drops at a slower rate from 32 to 180 Hz since the film cooling effectiveness in Regime I (0–180 Hz) are mostly governed by the jet lift-off at the high-velocity magnitude part of the cycle and further jet lift-off does not bring as much decrease in film cooling effectiveness as between 16 and 32 Hz. These observations could be confirmed from the mean temperature contours illustrated in Figure 17a–e. If the oscillation frequency goes from 16 to 32 Hz, less coolant contact with the wall is illustrated in Figure 17c,d, whereas there is no significant difference for the coolant contact with the wall between 32 and 180 Hz, as shown in Figure 17d,e. The experimental data from Seo et al. [7] is available up to 32 Hz and the LES results over-predict the centerline effectiveness and the under-predict the spanwise-averaged effectiveness as seen in Figures 14 and 15, even though the trends of the adiabatic film cooling effectiveness are close to the experimental data. The difference between the experimental data and the LES results for the centerline effectiveness are about 4–16%. Generally, LES results report much better predictions than the URANS results, however, even LES could not capture all the flow physics generated by the film cooling since complex vortical structures are generated by the mixing process between the main flow and the coolant jet in the narrow region near the film cooling hole. In Regime I (0–180 Hz), when the oscillation frequency goes from 0 to 2, 16, 32, 90, or 180 Hz, the centerline effectiveness decreases by about 10%, 12%, 47%, 58%, or 71% and the spanwise-averaged effectiveness drops by about 11%, 12%, 45%, 62%, or 75% respectively.

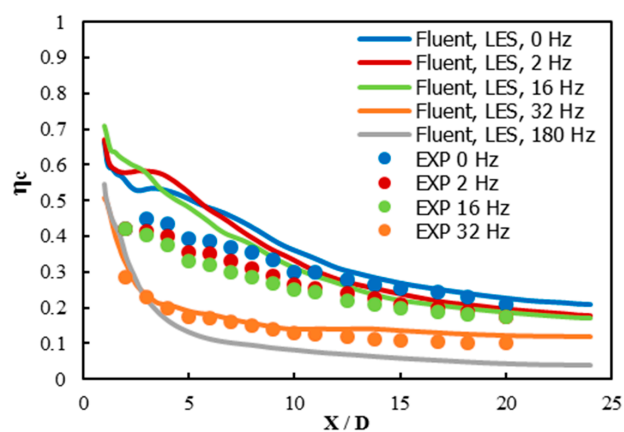


**Figure 14.** The centerline effectiveness obtained using the LES Smagorinsky–Lilly model for  $M = 0.5$  for the 0, 2, 16, 32, and 180 Hz oscillations.

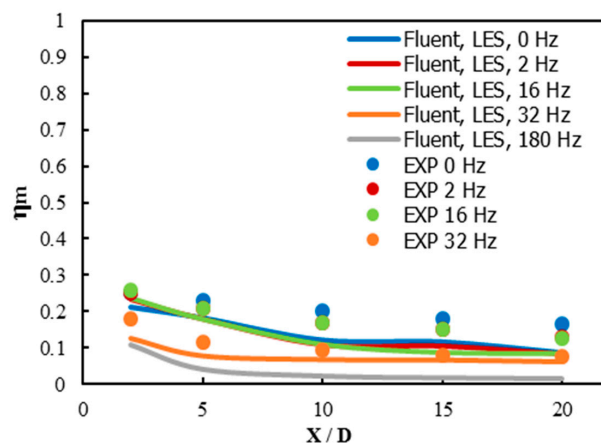


**Figure 15.** The spanwise-averaged effectiveness obtained using the LES Smagorinsky–Lilly model for  $M = 0.5$  for the 0, 2, 16, 32, and 180 Hz oscillations.

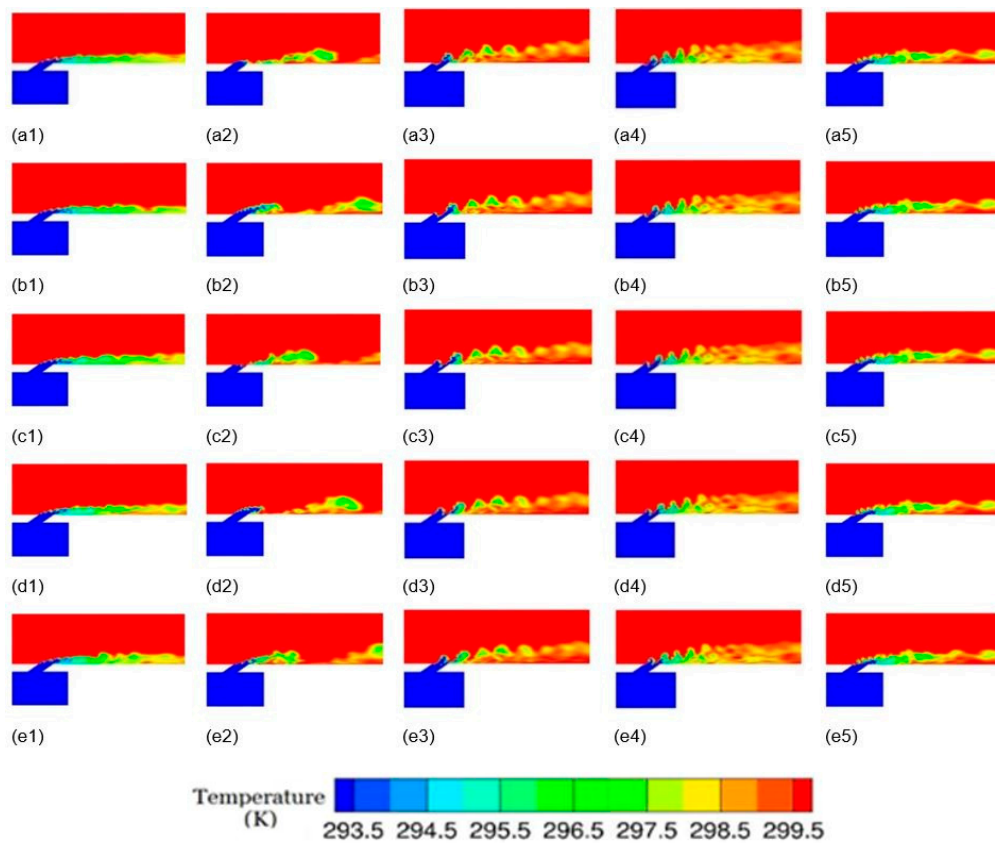


**Figure 16.** (a1–e1) The instantaneous temperature contours for the central cross section using the FLUENT, LES, Smagorinsky–Lilly model for  $M = 0.5$ , 2 Hz [28]. (a2–e2) The instantaneous temperature contours for the central cross section using the FLUENT, LES, Smagorinsky–Lilly model for  $M = 0.5$ , 32 Hz [28]. (a3–e3) The instantaneous temperature contours for the central cross section using the FLUENT, LES, Smagorinsky–Lilly model for  $M = 0.5$ , 180 Hz [28]. (a4–e4) The instantaneous temperature contours for the central cross section using the FLUENT, LES, Smagorinsky–Lilly model for  $M = 0.5$ , 268 Hz [28]. (a5–e5). The instantaneous temperature contours for the central cross section using the FLUENT, LES, Smagorinsky–Lilly model for  $M = 0.5$ , 536 Hz [28]. (a)  $t/\text{period} = 0$  (b)  $t/\text{period} = 0.2$  (c)  $t/\text{period} = 0.4$  (d)  $t/\text{period} = 0.6$  (e)  $t/\text{period} = 0.8$ .

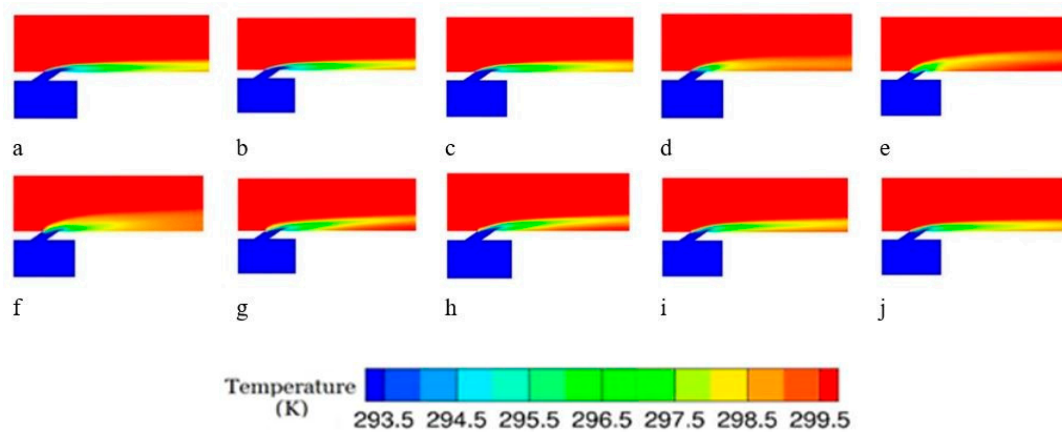


**Figure 17.** (a) The mean temperature contours for the central cross section using the FLUENT, LES, Smagorinsky–Lilly model for  $M = 0.5$ , 0 Hz [28]. (b) Mean temperature contours for the central cross section using the FLUENT, LES, Smagorinsky–Lilly model for  $M = 0.5$ , 2 Hz [28]. (c) Mean temperature contours for the central cross section using the FLUENT, LES, Smagorinsky–Lilly model for  $M = 0.5$ , 16 Hz [28]. (d) Mean temperature contours for the central cross section using the FLUENT, LES, Smagorinsky–Lilly model for  $M = 0.5$ , 32 Hz [28]. (e) Mean temperature contours for the central cross section using the FLUENT, LES, Smagorinsky–Lilly model for  $M = 0.5$ , 180 Hz [28]. (f) Mean temperature contour for the central cross section using the FLUENT, LES, Smagorinsky–Lilly model for  $M = 0.5$ , 268 Hz [28]. (g) Mean temperature contour for the central cross section using the FLUENT, LES, Smagorinsky–Lilly model for  $M = 0.5$ , 536 Hz [28]. (h) Mean temperature contour for the central cross section using the FLUENT, LES, Smagorinsky–Lilly model for  $M = 0.5$ , 1072 Hz [28]. (i) Mean temperature contour for central cross section using the FLUENT, LES, Smagorinsky–Lilly model for  $M = 0.5$ , 1608 Hz [28]. (j). Mean temperature contour for central cross section using the FLUENT, LES, Smagorinsky–Lilly model for  $M = 0.5$ , 2144 Hz [28].

#### 4.2.2. Stanton Number Ratio

When the oscillation frequency goes from 0 to 32 Hz, the mixing between the main flow and the coolant increases, resulting in the increase of the centerline and the spanwise-average Stanton number ratios as shown in Figures 18 and 19. In this frequency range (0–32 Hz), if the oscillation frequency increases, the amplitude of the static pressure oscillation between and around the film cooling hole exit and around the delivery tube inlet in the plenum increases. This leads to an increased amplitude of the coolant flow rate oscillations and more shear between the coolant jet and the main flow. Thus, the heat transfer coefficient and the Stanton number ratio increase. However, when the frequency increases from 32 to 180 Hz, the centerline and the spanwise-averaged Stanton number ratios increase slightly as illustrated in Figures 18 and 19. The coolant jet lift-off is the dominant phenomenon in this frequency range (32–180 Hz) and the entrainment of the main flow underneath the jet does not lead to the increase of mixing near the wall. As illustrated in Figure 18, the centerline Stanton number ratio could be partially less than 1. At a low average blowing ratio of  $M = 0.5$ , the coolant injection decreases the velocity gradients near the wall in the centerline. This leads to less turbulence production resulting in the centerline Stanton number ratios of less than 1. If the frequency is increased from 0 Hz to 2, 16, 32, or 180 Hz, the DES results show the centerline Stanton number ratio increases by about 3%, 5%, 8%, or 10% and the spanwise-averaged Stanton number ratio increases by about 0.3%, 1%, 3.7%, or 4.1% and the trends of the effectiveness are close to the experimental data.

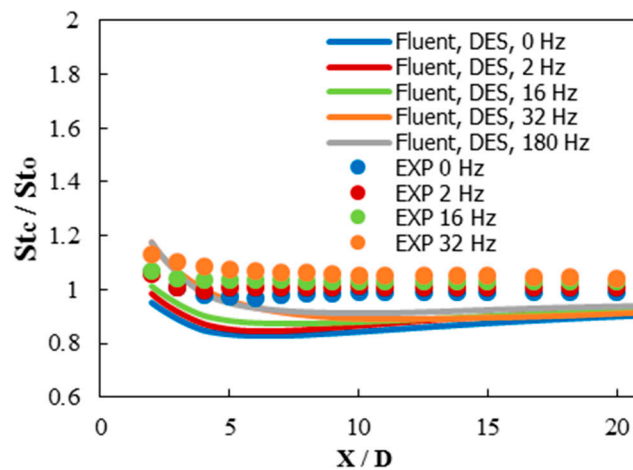


**Figure 18.** The centerline Stanton number ratio obtained using the DES Realizable  $k-\epsilon$  model for  $M = 0.5$  for the 0, 2, 16, 32, and 180 Hz oscillations.

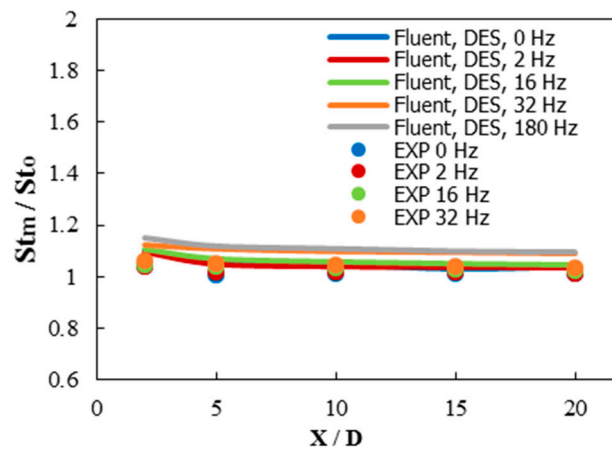


**Figure 19.** The spanwise-averaged Stanton number ratio obtained using the DES Realizable  $k-\epsilon$  model for  $M = 0.5$  for the 0, 2, 16, 32, and 180 Hz oscillations.

### 4.3. Regime II for $M = 0.5$ : 180–268 Hz

#### 4.3.1. Film Cooling Effectiveness

When the oscillation frequencies of the main flow and coolant jet are increased from 180 to 268 Hz, the centerline and the spanwise-averaged effectiveness increase significantly as illustrated in Figures 20 and 21. Figure 12 also shows the spanwise-averaged film cooling effectiveness at  $X/D = 7$  increases sharply between 180 and 268 Hz. At 268 Hz, the large vortices of coolant created during the high-velocity magnitude of the cycle overlap the thin coolant film near the wall created during the low-velocity magnitude part of the cycle [24]. At 180 Hz, large vortices could be distinguished at enough intervals as shown in Figure 16(a3–e3). The large vortices of coolant move closer together at 268 Hz and prevent the thin coolant film from mixing with the hot main flow, as seen in Figure 16(a3–e3, a4–e4). The entrainment of the main flow under the jet is not induced and the film cooling effectiveness increases. These observations could be confirmed from the mean temperature contours in Figure 17e,f, where, if the oscillation frequency increases in Regime II (180–268 Hz), coolant contact with the wall increases. When the frequency goes from 180 to 268 Hz, the centerline effectiveness increases by about 150% and the spanwise-averaged effectiveness climbs up by about 210%.

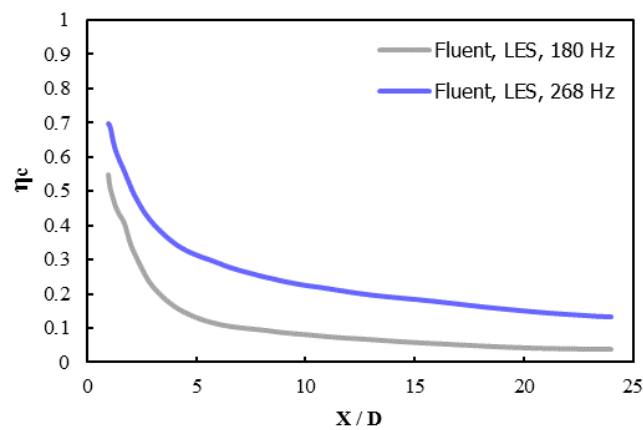


**Figure 20.** The centerline effectiveness obtained using the LES Smagorinsky–Lilly model for  $M = 0.5$  for the 180 and 268 Hz oscillations [28].

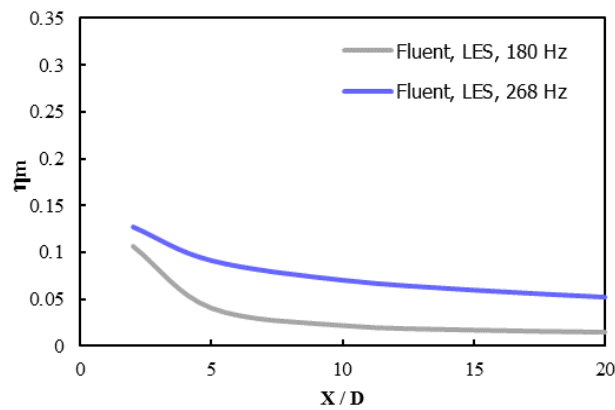


**Figure 21.** The spanwise-averaged effectiveness obtained using the LES Smagorinsky–Lilly model for  $M = 0.5$  for the 180 and 268 Hz oscillations [28].

#### 4.3.2. Stanton Number Ratio

If the frequency goes from 180 to 268 Hz, the centerline and the spanwise-averaged Stanton number ratios increase slightly as illustrated in Figures 22 and 23. As mentioned earlier, the coolant jet lift-off is the dominant phenomenon in this frequency range (32–536 Hz) and the entrainment of the hot main flow under the coolant jet does not lead to the increase of mixing near the wall. If the frequency is increased from 180 to 268 Hz, the DES results show the centerline Stanton number ratio increases by about 2% and the spanwise-averaged Stanton number ratio increases by about 1%.

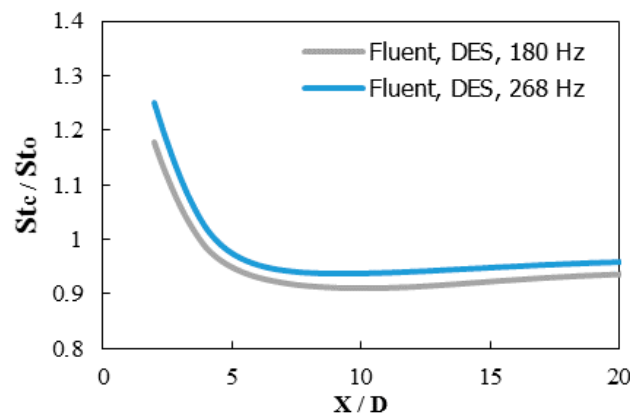


**Figure 22.** The centerline Stanton number ratio obtained using the DES Realizable  $k-\epsilon$  model for  $M = 0.5$  for the 180 and 268 Hz oscillations.

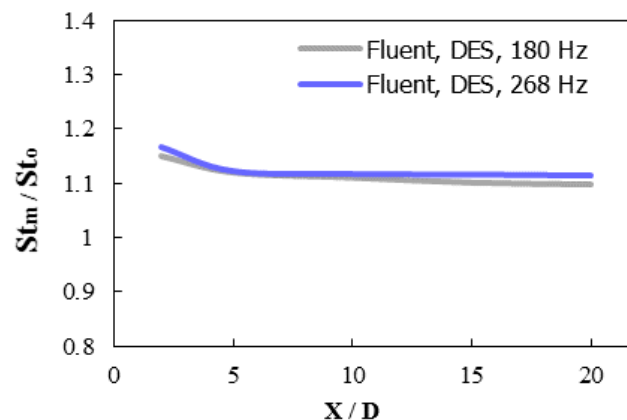


**Figure 23.** The spanwise-averaged Stanton number ratio obtained using the DES Realizable  $k-\epsilon$  model for  $M = 0.5$  for the 180 and 268 Hz oscillations.

#### 4.4. Regime III for $M = 0.5$ : 268–1072 Hz

##### 4.4.1. Film Cooling Effectiveness

If the oscillation frequencies of the main flow and the coolant jet goes from 268 to 1072 Hz, the centerline and the spanwise-averaged film cooling effectiveness decrease as seen in Figures 24 and 25. If the velocity oscillation frequency is increased at the main and the plenum inlets, the frequency of the coolant injection frequency at the hole exit increases. In Regime III (268–1072 Hz), if the coolant injection frequency is increased, the large vortices of the coolant catch up with each other up to a certain downstream location because of the convection velocity of the vortices (the velocity of the main flow) is the constant. After this location, the large vortices are merged and could not be distinguished anymore, therefore, they behave like a layer as seen in Figures 16(a4–e4, a5–e5) and 26a. The component of the jet momentum at the high-velocity magnitude of the cycle lifts the merged vortices of the coolant up. Therefore, the entrainment of the hot main flow under the jet is induced leading to a decrease of the film cooling effectiveness. When the oscillation frequency is increased, the coolant injection frequency increases and the location where large vortices start merging gets closer to the trailing edge of the film cooling hole leading to decrease of the film cooling effectiveness because of the lift up of the merged vortices of the coolant as seen in Figures 16(a4–e4, a5–e5) and 26a. When the frequency goes from 268 Hz to 536, 804, or 1072 Hz, the centerline effectiveness decreases by about 45%, 52%, or 57% and the spanwise-averaged effectiveness drops by about 59%, 63%, or 67% respectively.

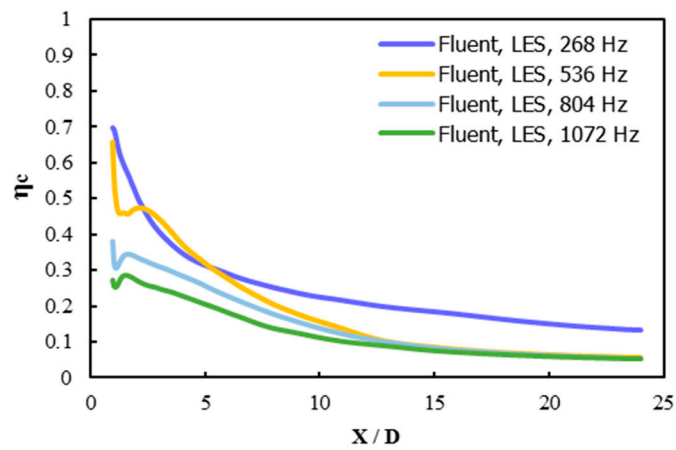


**Figure 24.** The centerline effectiveness obtained using the LES Smagorinsky–Lilly model for  $M = 0.5$  for the 268, 536, 804, and 1072 Hz oscillations [28].

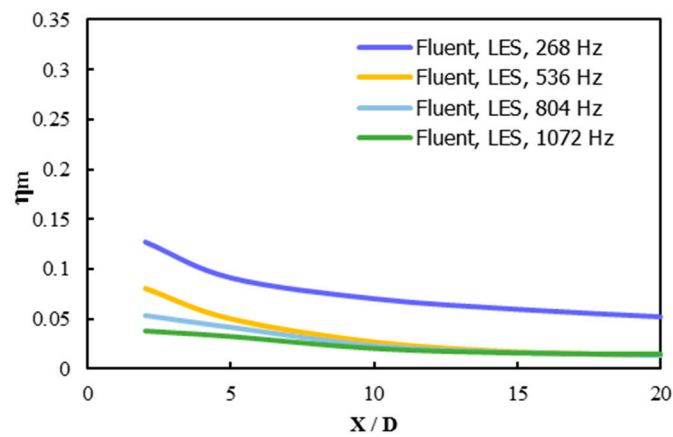


**Figure 25.** The spanwise-averaged effectiveness obtained using the LES Smagorinsky–Lilly model for  $M = 0.5$  for the 268, 536, 804, and 1072 Hz oscillations [28].

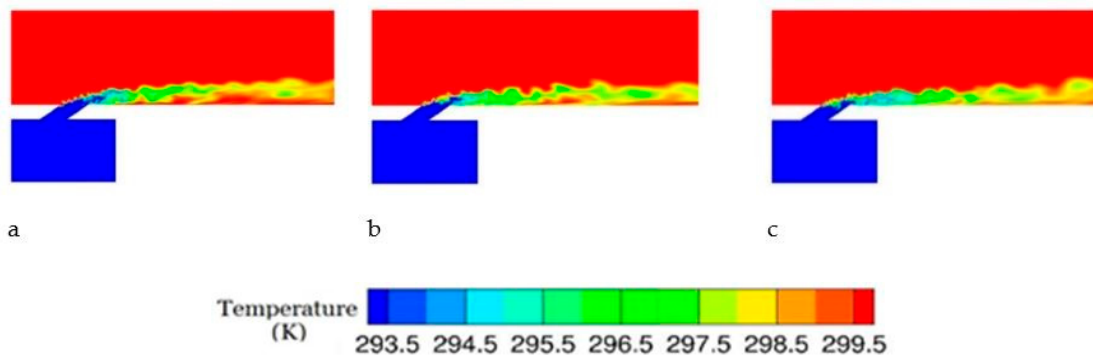


**Figure 26.** (a) The instantaneous temperature contour for the central cross section using the FLUENT, LES, Smagorinsky–Lilly model for  $M = 0.5$ , 1072 Hz (b). [28] The instantaneous temperature contour for the central cross section using the FLUENT, LES, Smagorinsky–Lilly model for  $M = 0.5$ , 1608 Hz (c). [28] The instantaneous temperature contour for the central cross section using the FLUENT, LES, Smagorinsky–Lilly model for  $M = 0.5$ , 2144 Hz [28].

#### 4.4.2. Stanton Number Ratio

When the frequency is increased from 268 to 804 Hz, the centerline Stanton number ratios are almost the constant and the spanwise-averaged Stanton number ratios increase slightly as illustrated in Figures 27 and 28 since the entrainment of the main flow underneath the jet does not lead to a great increase of mixing near the wall. If the frequency is increased from 268 Hz to 536, or 804 Hz, the DES results show that the centerline Stanton number ratio increases by about 0.4%, or 0.6% and the spanwise-averaged Stanton number ratio increases by about 2.0%, or 2.1%.

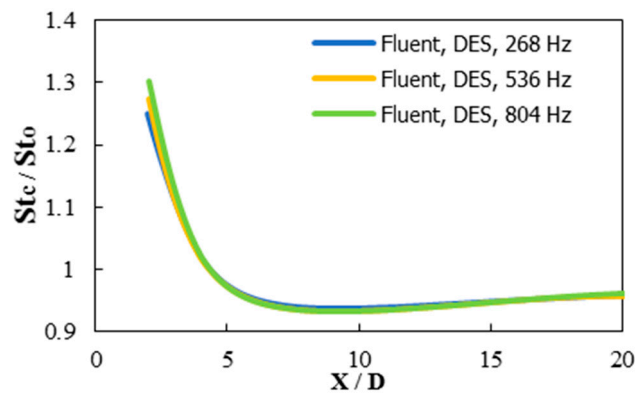


**Figure 27.** The centerline Stanton number ratio obtained using the DES Realizable  $k-\epsilon$  model for  $M = 0.5$  for the 268, 536, and 804 Hz oscillations.

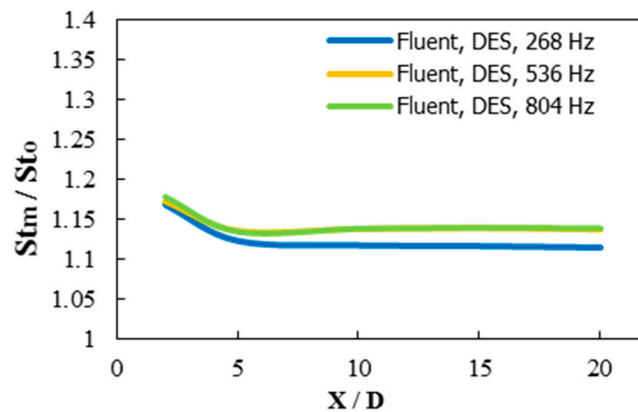


**Figure 28.** The spanwise-averaged Stanton number ratio obtained using the DES Realizable  $k-\epsilon$  model for  $M = 0.5$  for the 268, 536, and 804 Hz oscillations.

#### 4.5. Regime IV for $M = 0.5$ : 1072–2144 Hz

##### 4.5.1. Film Cooling Effectiveness

If the oscillation frequency of the main flow and coolant jet goes from 1072 to 2144 Hz, the centerline and the spanwise-averaged film cooling effectiveness increase, as illustrated in Figures 29 and 30. When the frequency exceeds 1072 Hz, the coolant jet could not respond to the flow oscillations as quickly due to tiny period compared to the time for the main flow to cross the hole exit. The time for the jet to lift the merged vortices of the coolant up at the high-velocity magnitude of the cycle gets reduced leading to decreased jet lift-off. If the frequency goes from 1072 to 2144 Hz, the injected coolant touches the wall more at the low-velocity magnitude of the cycle leading to an increase of film cooling effectiveness. These observations could be confirmed from Figures 17h–j and 26. In these figures, if the frequency increases from 1072 to 2144 Hz, more coolant contact with the wall is observed. Thus, the behavior of the cooling jet at 2144 Hz is very similar to that at 0 Hz leading to the difference

in the film cooling effectiveness with that at 0 Hz decreases. When the frequency goes from 1072 Hz to 1340, 1608, 1876, or 2144 Hz, the centerline effectiveness climbs up about 4%, 45%, 97%, or 105% and the spanwise-averaged effectiveness increases by about 7%, 97%, 192%, or 273%.

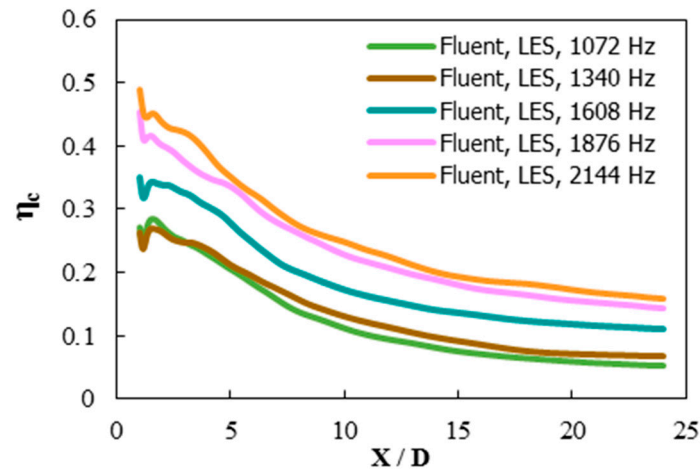


**Figure 29.** The centerline effectiveness obtained using the LES Smagorinsky–Lilly model for  $M = 0.5$  for the 1072, 1340, 1608, 1876, and 2144 Hz oscillations [28].

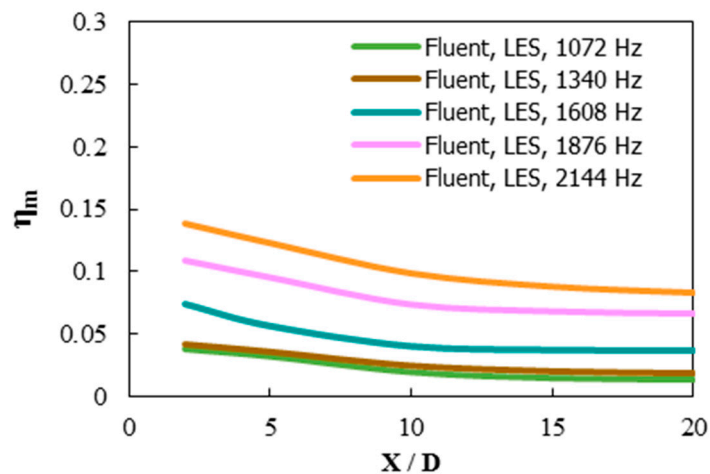


**Figure 30.** The spanwise-averaged effectiveness obtained using the LES Smagorinsky–Lilly model for  $M = 0.5$  for the 268, 536, 804, and 1072 Hz oscillations [28].

#### 4.5.2. Stanton Number Ratio

If the frequency exceeds 804 Hz, the centerline and spanwise-averaged Stanton number ratio decrease as shown in Figures 31 and 32 since the coolant responds less to the oscillations and disturbances are generated. If the frequency is increased from 1072 Hz to 1340, 1608, 1876, or 2144 Hz, the DES results show the centerline Stanton number ratio decreases by about 0.3%, 0.5%, 0.6%, or 0.8% and the spanwise-averaged Stanton number ratio decreases by about 1%, 2%, 2.3%, or 3%.

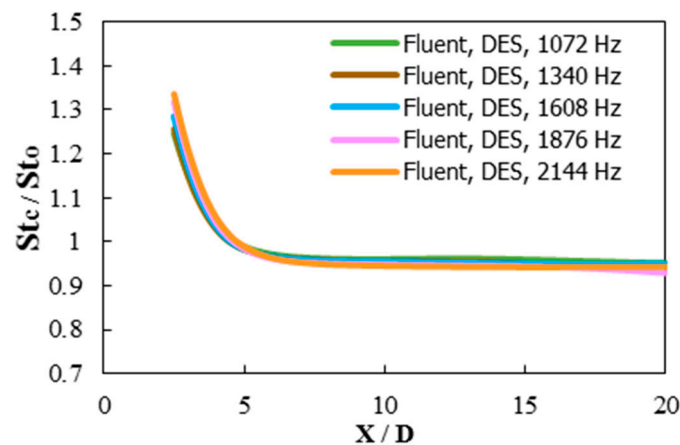


**Figure 31.** The centerline Stanton number ratio obtained using the DES Realizable  $k-\epsilon$  model for  $M = 0.5$  for the 1072, 1340, 1608, 1876, and 2144 Hz oscillations.

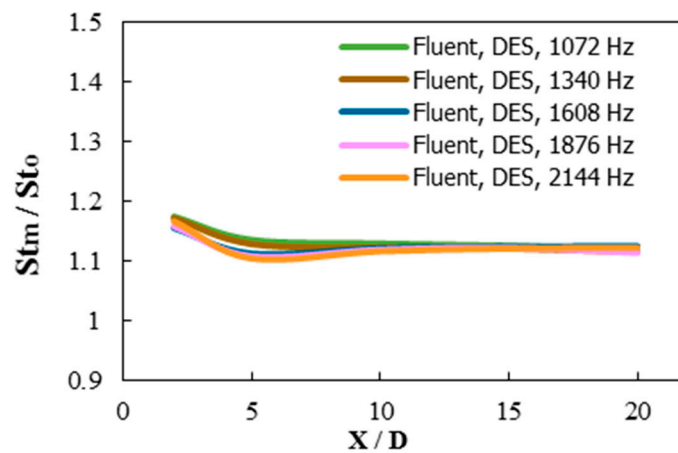


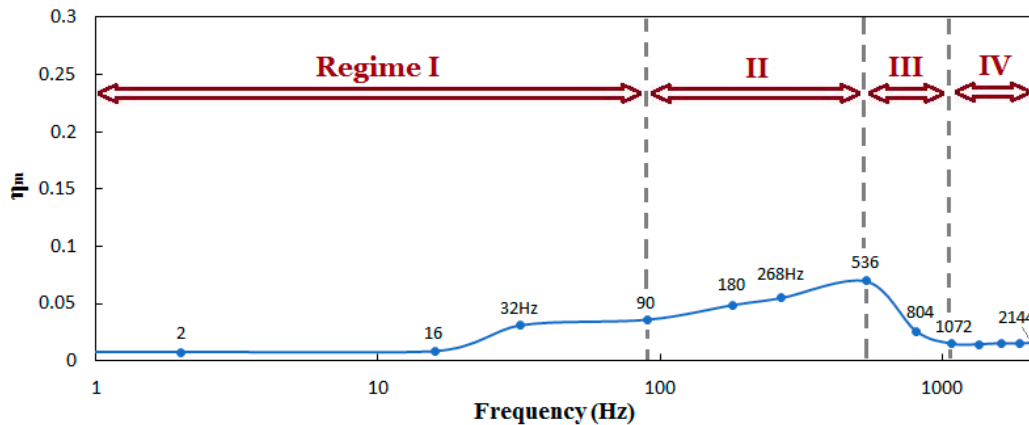
**Figure 32.** The spanwise-averaged Stanton number ratio obtained using the DES Realizable  $k-\epsilon$  model for  $M = 0.5$  for the 1072, 1340, 1608, 1876, and 2144 Hz oscillations.

In Equation (8), the C and D values at high frequencies are extrapolated with by using the linear characteristic as shown in Figure 10 since the experimental data from Seo et al. [7] is available up to 32 Hz and no other experimental data at higher frequencies is available at this point. As discussed up to this point, in the Regimes II, III, and IV, the film cooling effectiveness is dominated by the coolant injection frequency and the convection velocity of the vortices (=main flow velocity). Therefore, small variations of A and B values in Equations (5) and (7) have little effect on the film cooling effectiveness. Thus, it could be justified that the C and D values in Equation (8) at high frequencies are extrapolated with using the linear characteristic.

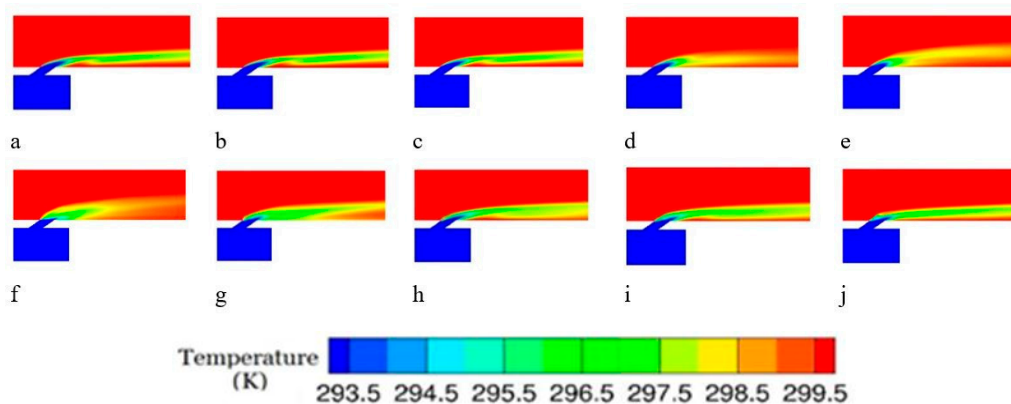
#### 4.6. Average Blowing Ratio $M = 1.0$

Figure 33 shows that the results of the spanwise-averaged film cooling effectiveness at  $X/D = 7$  as a function of frequency at the average blowing ratio of  $M = 1.0$  and four distinct regimes (Regime I, II, III, and IV) can be identified for the behavior of adiabatic film cooling effectiveness like  $M = 0.5$ . The trends of the effectiveness at the average blowing ratio  $M = 1.0$  are similar with those at the average blowing ratio  $M = 0.5$ , except from 0 to 90 Hz (Regime I) as shown in Figures 34 and 35. When the oscillation frequency rises from 0 to 90 Hz (Regime I), the spanwise-average film cooling effectiveness increases. Figure 36 shows the results of the spanwise-averaged Stanton number ratio at  $X/D = 7$  as a function of frequency at the average blowing ratio of  $M = 1.0$ . The trends of the Stanton number ratio at the average blowing ratio  $M = 1.0$  are also similar with those at the average blowing ratio  $M = 0.5$

except from 0 to 90 Hz (Regime I). In Regime I, when the oscillation frequency increases, the Stanton number ratio decreases. The details will be discussed in the next sections. As illustrated in Figure 33, at  $M = 1.0$ , if the oscillation frequency is increased in Regime IV, the film cooling effectiveness becomes similar to that at 0 Hz like  $M = 0.5$  in Figure 12. However, the film cooling effectiveness at 1072 Hz at  $M = 1.0$  is already similar to that at 0 Hz as shown in Figure 33. Therefore, the film cooling effectiveness is almost constant in Regime IV.



**Figure 33.** The variation of the spanwise-averaged effectiveness in terms of frequency (Hz) at  $X/D = 7$  for  $M = 1.0$  obtained by the FLUENT, LES, Smagorinsky–Lilly model. The orange color point is the result for the multi-frequency unsteady flow. It represents the spanwise-averaged film cooling effectiveness when Equations (28) and (29) are used instead of individual frequencies.



**Figure 34.** (a) The mean temperature contours for the central cross section using the FLUENT, LES, Smagorinsky–Lilly model for  $M = 1.0$ , 0 Hz. (b) The mean temperature contours for the central cross section using the FLUENT, LES, Smagorinsky–Lilly model for  $M = 1.0$ , 2 Hz. (c) The mean temperature contours for the central cross section using the FLUENT, LES, Smagorinsky–Lilly model for  $M = 1.0$ , 16 Hz. (d) The mean temperature contours for the central cross section using the FLUENT, LES, Smagorinsky–Lilly model for  $M = 1.0$ , 32 Hz. (e) The mean temperature contours for the central cross section using the FLUENT, LES, Smagorinsky–Lilly model for  $M = 1.0$ , 90 Hz. (f) The mean temperature contour for the central cross section using the FLUENT, LES, Smagorinsky–Lilly model for  $M = 1.0$ , 268 Hz. (g) The mean temperature contour for the central cross section using the FLUENT, LES, Smagorinsky–Lilly model for  $M = 1.0$ , 536 Hz. (h) The mean temperature contour for the central cross section using the FLUENT, LES, Smagorinsky–Lilly model for  $M = 1.0$ , 1072 Hz. (i) The mean temperature contour for the central cross section using the FLUENT, LES, Smagorinsky–Lilly model for  $M = 1.0$ , 1608 Hz. (j) The mean temperature contour for the central cross section using the FLUENT, LES, Smagorinsky–Lilly model for  $M = 1.0$ , 2144 Hz.

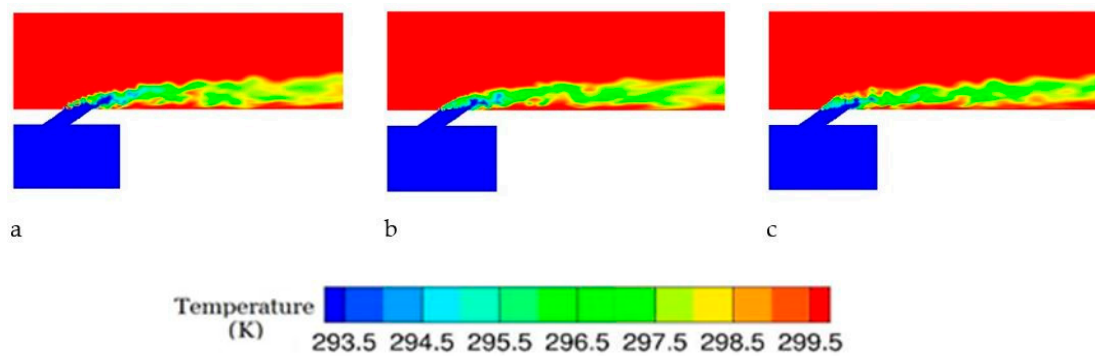


**Figure 35.** (a) The instantaneous temperature contour at the central cross section obtained using FLUENT, LES, Smagorinsky–Lilly model for  $M = 1.0$ , 1072 Hz. (b) The instantaneous temperature contour for the central cross section obtained using FLUENT, LES, Smagorinsky–Lilly model for  $M = 1.0$ , 1608 Hz. (c) The instantaneous temperature contour for the central cross section obtained using FLUENT, LES, Smagorinsky–Lilly model for  $M = 1.0$ , 2144 Hz.

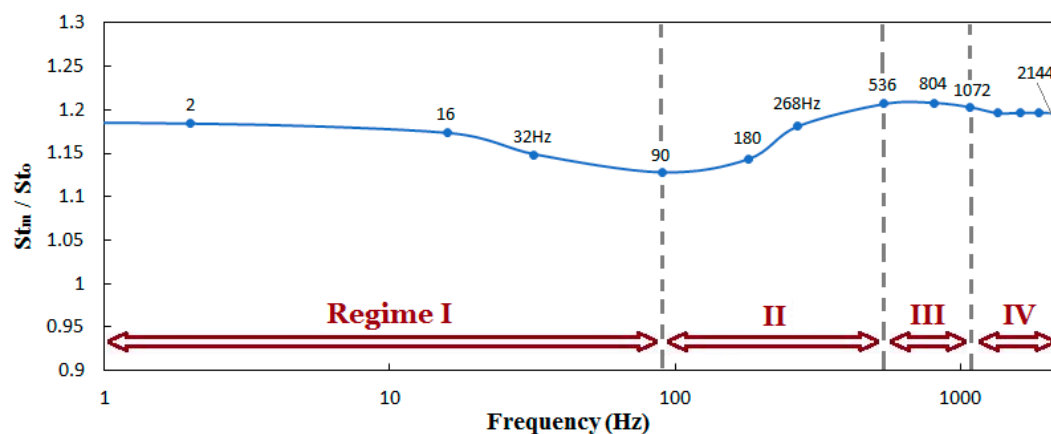


**Figure 36.** The variation of the spanwise-averaged Stanton number ratio in terms of frequency (Hz) at  $X/D = 7$  for  $M = 1.0$  obtained by the FLUENT, DES, Realizable  $k$ - $\epsilon$  model. The orange color point is the result for the multi-frequency unsteady flow. It represents the spanwise-averaged film cooling effectiveness when Equations (28) and (29) are used instead of individual frequencies.

#### 4.7. Regime I for $M = 1.0$ : 0–90 Hz

##### 4.7.1. Film Cooling Effectiveness

At the average blowing ratio of  $M = 1.0$ , if the frequencies of the mainstream and the coolant jet increase from 0 to 90 Hz, the centerline and the spanwise-averaged film cooling effectiveness increase as seen in Figures 37 and 38, respectively. As shown in Figure 33, the spanwise-averaged effectiveness at  $X/D = 7$  shows a very slight increase between 0 and 16 Hz and a large jump between 16 and 32 Hz. Like  $M = 0.5$ , if the oscillation frequency of the main flow and the coolant jet increases at the average blowing ratio of  $M = 1.0$ , the amplitude of the static pressure difference between the mainstream and the coolant plenum increases and the coolant flow rate oscillation amplitude also increases [45]. Because of the oscillating momentum of the coolant jet, the angle of the coolant jet after it comes out of the hole changes periodically and coolant flapping is generated. If the frequency is increased, the possibility of coolant contact with the wall increases. However, up to 16 Hz, the possibility of the contact is still low and the film cooling effectiveness very slightly increases as shown in Figures 36 and 37. If the oscillation frequency goes from 16 to 32 Hz, the oscillation amplitude of the angle of the coolant injection becomes higher and the possibility of the cooling jet contact with the wall increases significantly and it touches the wall periodically. Therefore, a sharp increase in the

effectiveness is observed between 16 to 32 Hz in Figures 39(a2–e2) and 34d. Between 32 and 90 Hz, the increase of the film cooling effectiveness continues at a slower rate because, in this frequency range, the effectiveness values are mostly governed by the coolant flapping and further coolant flapping does not bring as much increase in the film cooling effectiveness as between 16 to 32 Hz. These observations can also be confirmed from the mean temperature contours in Figure 34d,e. Figures 39(a2–e2) and 34d show that if the frequency is increased from 16 to 32 Hz, there is more coolant contact with the wall. However, there is no substantial difference for the coolant contact between 32 and 90 Hz as seen in Figures 39(a3–e3) and 34e. In this regime, when the frequency goes from 0 Hz to 2, 16, 32, or 90 Hz at  $M = 1.0$ , the centerline effectiveness increases by about 8%, 19%, 320%, or 332% and the spanwise-averaged effectiveness increases by about 10%, 29%, 330%, or 345% respectively.

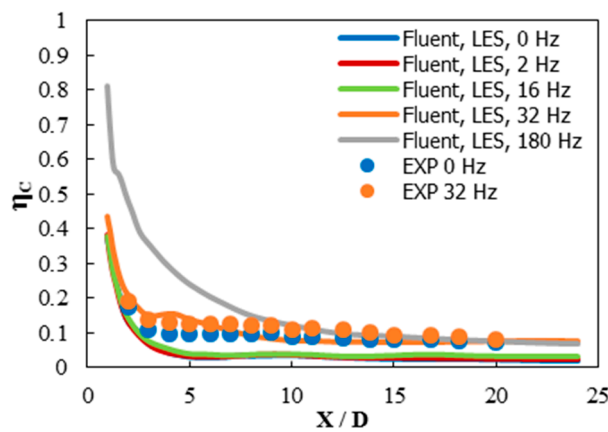


**Figure 37.** The centerline effectiveness obtained using the LES Smagorinsky–Lilly model for  $M = 1.0$  for the 0, 2, 16, 32, and 180 Hz oscillations.

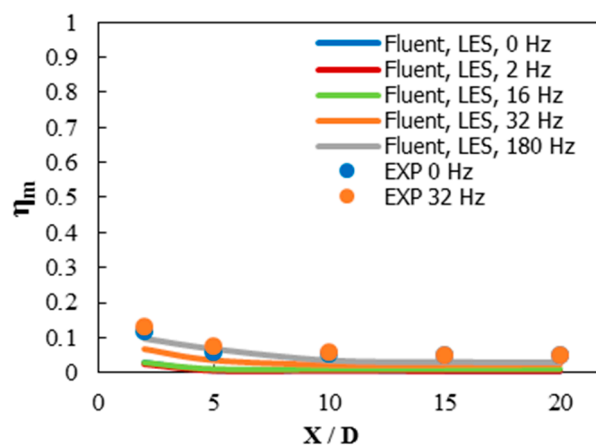


**Figure 38.** The spanwise-averaged effectiveness obtained using the LES Smagorinsky–Lilly model for  $M = 1.0$  for the 0, 2, 16, 32, and 180 Hz oscillations.

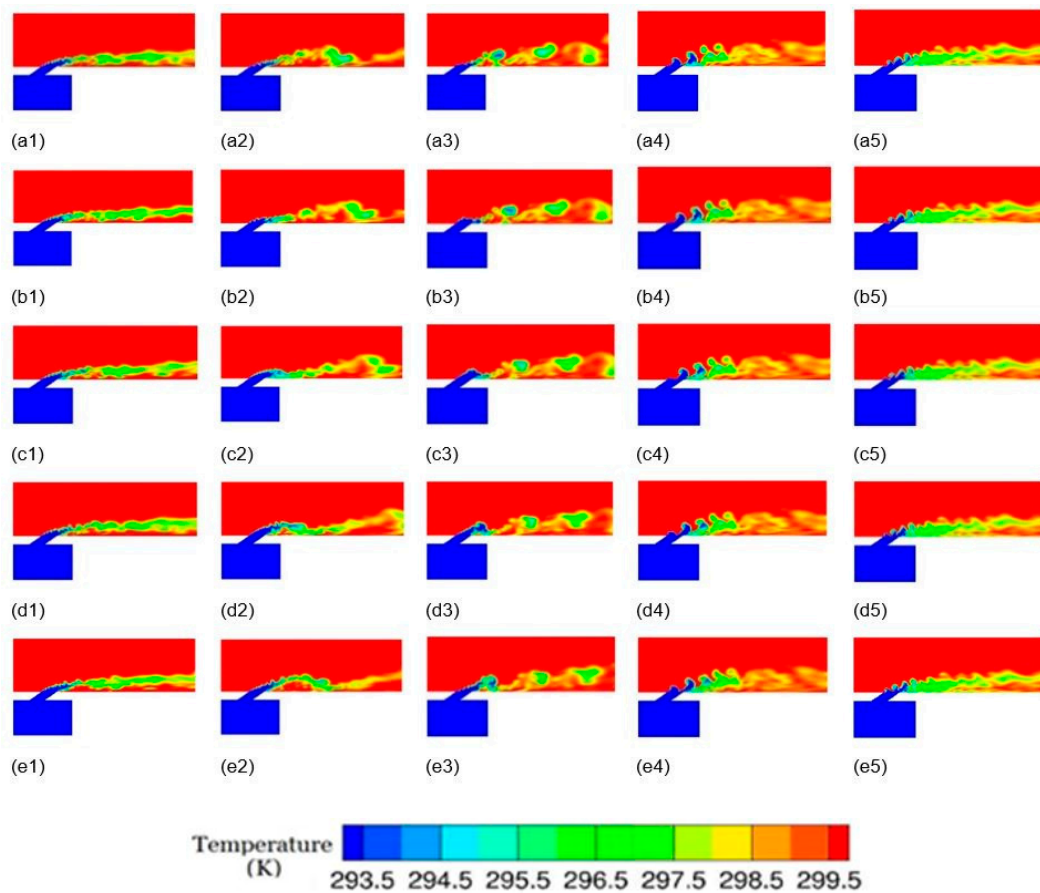


**Figure 39.** (a1–e1) The instantaneous temperature contours for the central cross section using the FLUENT, LES, Smagorinsky–Lilly model for  $M = 1.0$ , 2 Hz. (a2–e2) The instantaneous temperature contours for the central cross section using the FLUENT, LES, Smagorinsky–Lilly model for  $M = 1.0$ , 32 Hz. (a3–e3) The instantaneous temperature contours for the central cross section using the FLUENT, LES, Smagorinsky–Lilly model for  $M = 1.0$ , 90 Hz. (a4–e4) The instantaneous temperature contours for the central cross section using the FLUENT, LES, Smagorinsky–Lilly model for  $M = 1.0$ , 268 Hz. (a5–e5) The instantaneous temperature contours for the central cross section using the FLUENT, LES, Smagorinsky–Lilly model for  $M = 1.0$ , 536 Hz. (a)  $t/\text{period} = 0$  (b)  $t/\text{period} = 0.2$  (c)  $t/\text{period} = 0.4$  (d)  $t/\text{period} = 0.6$  (e)  $t/\text{period} = 0.8$ .

#### 4.7.2. Stanton Number Ratio

The centerline and the spanwise-averaged Stanton number ratios obtained using the DES model as a function of  $X/D$  at the high average blowing ratio of  $M = 1.0$  are illustrated in Figures 40 and 41. The coolant injection causes a disturbance in the main flow by the interaction between the jet and the mainstream and increases the heat transfer coefficients and the Stanton number. At high average blowing ratios of  $M = 1.0$ , the spanwise-averaged Stanton number ratio shows the maximum values at the downstream region as seen in Figure 41 since the maximum disturbance is created around the region where the injected coolant re-attaches to the wall periodically. Since the most disturbance is generated in the downstream region, the spanwise-averaged Stanton number ratio increases as  $X/D$  increases. If the oscillating frequency of the main flow and the jet increases from 0 to 180 Hz, the spanwise-averaged Stanton number decreases as shown in Figure 41.

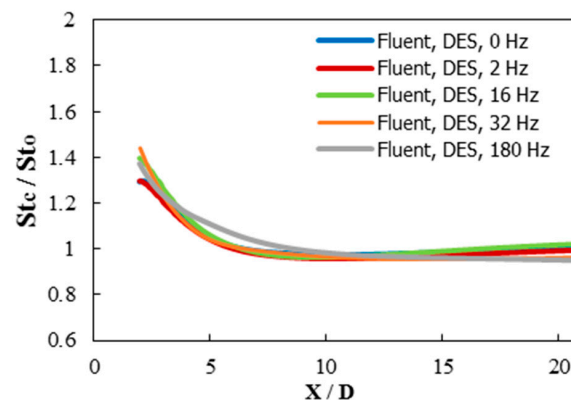


**Figure 40.** The centerline Stanton number ratio obtained using the DES Realizable  $k-\epsilon$  model for  $M = 0.5$  for the 0, 2, 16, 32, and 180 Hz oscillations.

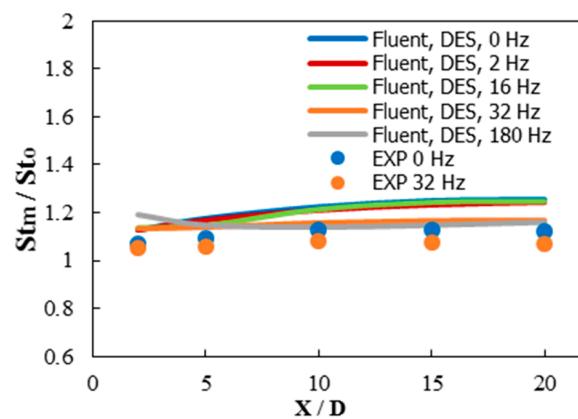


**Figure 41.** The spanwise-averaged Stanton number ratio obtained using the DES Realizable  $k-\epsilon$  model for  $M = 0.5$  for the 0, 2, 16, 32, and 180 Hz oscillations.

As mentioned earlier, at a high blowing ratio of  $M = 1.0$ , the coolant jet lift-off is generated under steady flow conditions (0 Hz), resulting in the entrainment of hot mainstream gases underneath the jet. The entrainment does not lead to much mixing near the wall [46]. If the oscillation frequency is increased from 0 to 90 Hz, more entrainment is induced under the cooling jet resulting in less disturbance and a lower increase of the heat transfer coefficient or the Stanton number ratio. However, if the frequency goes from 0 to 90 Hz, the centerline Stanton number stays almost constant, as seen in Figure 40, because the mixing between the main flow and the coolant is no longer increased near the wall at the centerline. When the frequency goes from 0 Hz to 2, 16, 32 or 90 Hz at  $M = 1.0$ , the centerline Stanton number ratio decreases by about 0.2%, 0.3%, 0.5%, or 0.5% and the spanwise-averaged Stanton number ratio decreases by about 1%, 1.2%, 7%, or 8%.

#### 4.8. Effects of Multi-Frequency Unsteady Flow

Multi-frequency velocities at the main inlet and the plenum inlet at the average blowing ratios of  $M = 0.5$  and 1.0 given by Equations (28) and (29) are applied to explore the effects of multi-frequency unsteady flows. The results at  $X/D = 7$  for the spanwise-averaged film cooling effectiveness obtained by the LES, Smagorinsky–Lilly model and the Stanton number ratio obtained by the DES, Realizable  $k-\epsilon$  model at  $M = 0.5$  and 1.0 are plotted with orange color points in Figures 12, 13, 33, and 34 respectively and compared to those at single frequencies. In these figures, the spanwise-averaged effectiveness and the Stanton number ratio for the multi-frequency flow is almost the average of the spanwise-averaged effectiveness and the Stanton number ratios obtained for single frequency flows at 1072 and 2144 Hz. This is somewhat expected because the Fourier analysis showed that the range of

the most dominant frequencies of the combustor unsteady pressure data was in between 1072 and 2144 Hz. The total weights calculated by the Fourier analysis of the experimental data in Figure 11 for cosine terms between 1072 and 2144 Hz are 92.5% and for sine terms between 1072 and 2144 Hz are 95.2%, as indicated in Table 7. The most important factor governing the dominant frequencies is the mass flow rate through the combustor, which is closely related to the gas turbine power [47]. In the experiment, the inner diameter and the length of the combustion chamber were 0.12 m and 0.85 m, respectively, and the air mass flow rate was 30 g/s [18]. It seems like this air mass flow rate and the size of the combustion chamber governed the dominant frequencies.

## 5. Conclusions

The effects of oscillations in the main flow and the coolant jet on film cooling at various frequencies from 0 to 2144 Hz at the average blowing ratio of  $M = 0.5$  and 1.0 are investigated. Numerical simulations for a  $35^\circ$  inline injection with a cylindrical hole on a flat plate are conducted using the LES model for the film cooling effectiveness and the DES model for the Stanton number ratio. At the average blowing ratio of  $M = 0.5$ , the frequency range is classified into four regimes, I, II, III, and IV based on the behavior of the film cooling effectiveness. In Regime I (0–180 Hz) (Sr: 0–2.827), if the frequency is increased, the film cooling effectiveness decreases because of the enhancement of the jet lift-off and the entrainment of the hot mainstream fluid under the jet. In Regime II (180–268 Hz) (Sr: 2.827–4.21), if the frequency goes up, the effectiveness increases because of the large vortices of coolant prevent the thin coolant film near the wall from mixing with the hot main flow by forcing the thin coolant film downward towards the wall. In Regime III (268–1072 Hz) (Sr: 4.21–16.839), when the frequency increases, the effectiveness drops because the vertical component of the jet force lifts the coolant from the wall and the entrainment of the hot main flow underneath the jet is induced. In Regime IV (1072–2144 Hz) (Sr: 16.839–33.678), if the frequency is increased, the effectiveness increases because the jets cannot respond to the flow oscillations as quick and the coolant behaves like at 0 Hz gradually. The trends of the effectiveness at high blowing ratio of  $M = 1.0$  are similar with those at  $M = 0.5$  except for Regime I. In Regime I (0–90 Hz) at  $M = 1.0$ , if the frequency is increased, the effectiveness increases due to an increased generation of the coolant flapping.

In terms of Stanton number ratio, at  $M = 0.5$ , if the frequency rises from 0 to 804 Hz, the spanwise-averaged Stanton number ratio goes up due to an increased flow disturbance near the wall. When the frequency exceeds 804 Hz, the spanwise-averaged Stanton number ratio is reduced since the jets do not respond to the high frequencies and return to the steady flow condition. The trends of the spanwise-averaged Stanton number ratio at  $M = 1.0$  are similar to those at  $M = 0.5$  except from 0 to 90 Hz. At  $M = 1.0$ , if the frequency is increased, the spanwise-averaged Stanton number ratio decreases because more entrainment of the main flow by the coolant flapping leads to less mixing near the wall. When multi-frequency unsteady flow obtained from a real combustor data is applied to the flow field, the film cooling effectiveness and the Stanton number ratio is almost the same as the average of the film cooling effectiveness and the Stanton number ratios for the dominant frequencies. Some representative results are as follows: at  $M = 0.5$ , if the oscillation frequency goes from 0 to 2, 16, 32, 90 or 180 Hz, the centerline effectiveness decreases by about 10%, 12%, 47%, 58%, or 71% and the spanwise-averaged effectiveness drops by about 11%, 12%, 45%, 62%, or 75% respectively. On the other hand, at  $M = 1.0$ , when the frequency goes from 0 Hz to 2, 16, 32, or 90 Hz, the centerline effectiveness increases by about 8%, 19%, 320%, or 332% and the spanwise-averaged effectiveness increases by about 10%, 29%, 330%, or 345% respectively. It can be said that it is important to include the effects of oscillating flows when designing film cooling systems for gas turbines.

**Author Contributions:** S.I.B. performed the CFD simulations, analyzed the data, and wrote the paper. S.Y. formulated and supervised the research, analyzed the data, and wrote the paper.

**Funding:** This research received no external funding.

**Conflicts of Interest:** The authors declare no conflict of interest.

## Nomenclature

---

$C_p$	Specific heat of fluid (J/kg·K)
$C_\mu$	Coefficient of eddy viscosity
$D$	Diameter of injection hole (m)
$f$	Frequency of oscillation (Hz)
$h_f$	Film heat transfer coefficient
$K$	Turbulent kinetic energy ( $W/m^2 \cdot K$ )
$L$	Delivery tube length (m)
$M$	Blowing ratio
$q_w$	Heat flux ( $W/m^2$ )
$Re_D$	Freestream Reynolds number based on the freestream velocity and hole diameter
$Sr$	Strouhal number (non-dimensional frequency)
$St_f$	Stanton number with film cooling
$St_C$	Centerline Stanton number
$St_m$	Spanwise-averaged Stanton number
$St_0$	Baseline Stanton number with no pulsations and no film cooling
$T_{aw}$	Adiabatic wall temperature (K)
$T_w$	Temperature of fluid-solid interface surface (K)
$u$	flow velocity (m/s)
$u'$	root-mean-square of the turbulent velocity fluctuations (m/s)
$u_C$	injectant velocity (m/s)
$U_G$	mainstream velocity (m/s)
$u^*$	Friction velocity (m/s)
$V$	Velocity (m/s)
$V_{main\_inlet}$	Velocity at the main inlet (m/s)
$V_{plenum\_inlet}$	Velocity at the plenum inlet (m/s)
$x$	Streamwise coordinate (m)
$x^+$	Dimensionless grid spacing in the x-direction
$y$	Wall-normal coordinate (m)
$y^+$	Dimensionless wall distance
$z$	Spanwise coordinate (m)
$z^+$	Dimensionless grid spacing in the z-direction
<i>Greek symbols</i>	
$\alpha$	Phase difference between the main flow velocity oscillation at the main inlet and the coolant flow velocity oscillation at the plenum inlet
$\epsilon$	Dissipation rate of turbulent kinetic energy ( $m^2/s^3$ )
$\eta$	Adiabatic film cooling effectiveness
$\eta_C$	Centerline film cooling effectiveness
$\eta_m$	Spanwise-averaged film cooling effectiveness
$\rho$	density ( $kg/m^3$ )
$\rho_C$	injectant density ( $kg/m^3$ )
$\rho_G$	mainstream density ( $kg/m^3$ )
$\Phi$	non-dimensional metal temperature
$\nu$	Local kinematic viscosity ( $m^2/s$ )
<i>Subscripts</i>	
aw	Adiabatic wall
c	Centerline
G	Main flow gas
m	Spanwise-averaged
<i>Abbreviations</i>	
DES	Detached eddy simulation
LES	Large Eddy Simulation
RANS	Reynolds-Averaged Navier–Stokes
URANS	Unsteady RANS

---

## References

1. Press information, Mitsubishi Heavy Industries. Available online: [www.mhi.com/news/story/1105261435.html](http://www.mhi.com/news/story/1105261435.html). (accessed on 22 October 2018).
2. Nickel Iron Alloy Comparison Chart. Available online: [www.nealloys.com/pdf/nickel-iron-periodic-table.pdf](http://www.nealloys.com/pdf/nickel-iron-periodic-table.pdf) (accessed on 22 October 2018).
3. Li, X.; Subbuswamy, G.; Zhou, J. Performance of gas turbine film cooling with backward injection. *Energy Power Eng.* **2013**, *5*, 132–137. [[CrossRef](#)]
4. Bogard, D.; Thole, K. Gas turbine film cooling. *J. Propul. Power* **2006**, *22*, 249–270. [[CrossRef](#)]
5. Giampaolo, A. *Gas Turbine Handbook, Principles and Practices*, 3rd ed.; Fairmont Press: Liburn, GA, USA, 2006.
6. Coatings for Turbine Blades. Available online: [www.phase-trans.msm.cam.ac.uk/2003/Superalloys/coatings/index.html](http://www.phase-trans.msm.cam.ac.uk/2003/Superalloys/coatings/index.html). (accessed on 22 October 2018).
7. Seo, H.J.; Lee, J.S.; Ligrani, P.M. The effect of injection hole length on film cooling with bulk flow pulsations. *Int. J. Heat Mass Transfer* **1998**, *41*, 3515–3528. [[CrossRef](#)]
8. Bogard, D.G. Airfoil Film Cooling. In *The Gas Turbine Handbook*; National Energy Technology Laboratory: Albany, NY, USA, 2006.
9. Kays, W.; Crawford, M.; Weigand, B. *Convective Heat and Mass Transfer*, 4th ed.; McGrawHill: New York, NY, USA, 2005.
10. Lieuwen, T. *Combustion Driven Oscillations in Gas Turbines*; Turbomachinery International: Norwalk, CT, USA, 2003.
11. Han, J.; Dutta, S.; Ekkad, S. *Gas Turbine Heat Transfer and Cooling Technology*, 2nd ed.; CRC Press: Boca Raton, FL, USA, 2013.
12. Li, S.; Rallabandi, A.; Han, J. Influence of unsteady wake with trailing edge coolant ejection on turbine blade film cooling. *J. Turbomach.* **2012**, *134*, 061026. [[CrossRef](#)]
13. Ou, S.; Han, J.; Mehendale, A.; Lee, C. Unsteady wake over a linear turbine blade cascade with air and CO<sub>2</sub> film injection: Part I—Effect on heat transfer coefficients. In Proceedings of the International Gas Turbine and Aeroengine Congress and Exposition, Cincinnati, OH, USA, 24–27 May 1993.
14. Womack, K.; Volino, R.; Schultz, M. Measurements in film cooling flows with periodic wakes. *J. Turbomach.* **2008**, *130*, 041008. [[CrossRef](#)]
15. Hunt, J.; Morrison, J. Eddy structure in turbulent boundary layers. *Eur. J. Mech. B Fluids* **2000**, *19*, 673–694. [[CrossRef](#)]
16. Mayhew, J.; Baughn, J.; Byerley, A. The effect of freestream turbulence on film cooling adiabatic effectiveness. *Int. J. Heat Fluid Flow* **2003**, *24*, 669–679. [[CrossRef](#)]
17. Blimbaum, J.; Zanchetta, M.; Akin, T.; Acharya, V.; O'Connor, J.; Noble, D.R.; Lieuwen, T. Transverse to longitudinal acoustic coupling processes in annular combustion chambers. *Int. J. Spray Combust. Dyn.* **2012**, *4*, 275–298. [[CrossRef](#)]
18. Zhang, H.; Zhang, X.; Zhu, M. Experimental Investigation of Thermoacoustic Instabilities for a Model Combustor with Varying Fuel Components. *J. Eng. Gas Turbines Power* **2012**, *134*, 031504. [[CrossRef](#)]
19. Baek, S.; Yavuzkurt, S. Effects of Oscillations in the Main Flow Due to Thermoacoustic Fields in a Gas Turbine Combustor on Film Cooling. In Proceedings of the ASME Turbo Expo, Seoul, Korea, 13–17 June 2016.
20. Bianchini, C.; Andrei, L.; Andreini, A. Numerical Benchmark of Nonconventional RANS Turbulence Models for Film and Effusion Cooling. *J. Turbomach.* **2013**, *135*, 041026. [[CrossRef](#)]
21. Acharya, S.; Leedom, D. Large Eddy Simulations of Discrete Hole Film Cooling with Plenum Inflow Orientation Effects. *J. Heat Transfer* **2013**, *135*, 011010. [[CrossRef](#)]
22. Coulthard, S.; Volino, R.; Flack, K. Effect of Jet Pulsing on Film Cooling—Part I: Effectiveness and Flow-Field Temperature Results. *ASME J. Turbomach.* **2007**, *129*, 232–246. [[CrossRef](#)]
23. Ekkad, S.; Ou, S.; Rivir, R. Effect of Jet Pulsation and Duty Cycle on Film Cooling from a Single Jet on a Leading Edge Model. *ASME J. Turbomach.* **2006**, *128*, 564–571. [[CrossRef](#)]
24. Nikitopoulos, D.; Acharya, S.; Oertling, J.; Muldoon, F. On Active Control of Film-cooling Flows. In Proceedings of the ASME Turbo Expo 2006, Barcelona, Spain, 8–11 May 2006.
25. El-Gabry, L.A.; Rivir, R.B. Effect of Pulsed Film Cooling on Leading Edge Film Effectiveness. *ASME J. Turbomach.* **2012**, *134*, 041005. [[CrossRef](#)]

26. Behrendt, T.; Gerendas, M. Characterization of the influence of moderate pressure fluctuations on the cooling performance of advanced combustor cooling concepts in a reacting flow. In Proceedings of the ASME Turbo Expo, Copenhagen, Denmark, 11–15 June 2012.
27. Seo, H.J.; Lee, J.S.; Ligrani, P.M. Effect of bulk flow pulsations on film cooling from different length injection holes at different blowing ratios. *J. Turbomach.* **1999**, *121*, 542–550. [[CrossRef](#)]
28. Baek, S.; Yavuzkurt, S. Effects of Oscillations in the Main Flow on Film Cooling at Various Frequencies at a Low Blowing Ratio. In Proceedings of the ASME Turbo Expo 2018, Oslo, Norway, 11–15 June 2018.
29. Farhadi-Azar, R.; Ramezanzadeh, M.; Taeibi-Rahni, M.; Salimi, M. Compound Triple Jets Film Cooling Improvements via Velocity and Density Ratios: Large Eddy Simulation. *J. Fluids Eng.* **2011**, *133*, 031202. [[CrossRef](#)]
30. Rozati, A.; Tafti, D. Large-eddy simulations of leading edge film cooling: Analysis of flow structures, effectiveness, and heat transfer coefficient. *Int. J. Heat Fluid Flow* **2008**, *29*, 1–17. [[CrossRef](#)]
31. Kim, S.; Hassan, I. Unsteady heat transfer analysis of a film cooling flow. In Proceedings of the 46th AIAA Aerospace Science Meeting and Exhibit, Reno, Nevada, 7–10 January 2008.
32. ANSYS FLUENT Theory Guide v.14. Available online: [www.ansys.com/products/fluids/ansys-fluent](http://www.ansys.com/products/fluids/ansys-fluent) (accessed on 22 October 2018).
33. Pointwise Version 16.04. Available online: [www.pointwise.com/doc/user-manual/index.html](http://www.pointwise.com/doc/user-manual/index.html) (accessed on 22 October 2018).
34. Iourokina, I.; Lele, S. Towards large eddy simulation of film cooling flows on a model turbine blade leading edge. In Proceedings of the 43rd AIAA Aerospace Sciences Meeting and Exhibit, Reno, NV, USA, 10–13 January 2005.
35. Peet, Y.; Lele, S. Near field of film cooling jet issued into a flat plate boundary layer: LES STUDY. In Proceedings of the ASME Turbo Expo 2008, Berlin, Germany, 9–13 June 2008.
36. Agata, Y.; Takahashi, T.; Sakai, E.; Nishino, K. Numerical simulation of heat transfer coefficient and film cooling performance influenced by the orientation of internal turbulence promoting ribs. *J. Therm. Sci. Technol.* **2013**, *8*, 488–503. [[CrossRef](#)]
37. White, F. *Fluid Mechanics*, 4th ed.; McGraw-Hill: New York, NY, USA, 1999.
38. Cengel, Y.; Cimbala, J. *Fluid Mechanics*, 3rd ed.; McGrawHill: New York, NY, USA, 2014.
39. Cebeci, T.; Shao, J.; Kafyke, F.; Laurendeau, E. *Computational Fluid Dynamics for Engineers*; Springer: Berlin, Germany, 2005.
40. Tannehill, J.; Anderson, D.; Pletcher, R. *Computational Fluid Mechanics and Heat Transfer*, 2nd ed.; Taylor & Francis: Didcot, UK, 1997.
41. Shih, T.-H.; Liou, W.; Shabbir, A.; Yang, Z.; Zhu, J. A New k-epsilon Eddy-Viscosity Model for High Reynolds Number Turbulent Flows—Model Development and Validation. *Comput. Fluids* **1995**, *24*, 227–238. [[CrossRef](#)]
42. Rao, S. Modeling of Turbulent Flows and Boundary Layer. In *Computational Fluid Dynamics*; Intech: London, UK, 2010; pp. 285–306.
43. Smagorinsky, J. General Circulation Experiments with the Primitive Equations. I. The Basic Experiment. *Mon. Weather Rev.* **1963**, *91*, 99–164. [[CrossRef](#)]
44. Lieuwen, T.; Torres, H.; Johnson, C.; Zinn, T. A Mechanism of Combustion Instability in Lean Premixed Gas Turbine Combustors. *J. Eng. Gas Turbines Power* **2000**, *123*, 182–189. [[CrossRef](#)]
45. Jung, I.; Lee, J. Effects of bulk flow pulsations on film cooling from spanwise oriented holes. In Proceedings of the ASME International Gas Turbine & Aeroengine Congress & Exhibition, Stockholm, Sweden, 2–5 June 1998.
46. Yavuzkurt, S.; Moffat, J.; Kays, W. Full coverage film cooling. Part 1. Three-dimensional measurements of turbulence structure. *J. Fluid Mech.* **1980**, *101*, 129–158. [[CrossRef](#)]
47. Lefebvre, A. *Gas Turbine Combustor*, 2nd ed.; CRC Press: Boca Raton, FL, USA, 1998.

